



# Mix-and-inject XFEL crystallography reveals gated conformational dynamics during enzyme catalysis

Medhanjali Dasgupta<sup>a</sup>, Dominik Budday<sup>b</sup>, Saulo H. P. de Oliveira<sup>c,d</sup>, Peter Madzelan<sup>a</sup>, Darya Marchany-Rivera<sup>e</sup>, Javier Seravalli<sup>a</sup>, Brandon Hayes<sup>f</sup>, Raymond G. Sierra<sup>f,g</sup>, Sébastien Boutet<sup>f</sup>, Mark S. Hunter<sup>f</sup>, Roberto Alonso-Mori<sup>f</sup>, Alexander Batyuk<sup>f</sup>, Jennifer Wierman<sup>h</sup>, Artem Lyubimov<sup>h</sup>, Aaron S. Brewster<sup>i</sup>, Nicholas K. Sauter<sup>i</sup>, Gregory A. Applegate<sup>i</sup>, Virendra K. Tiwari<sup>j</sup>, David B. Berkowitz<sup>j</sup>, Michael C. Thompson<sup>k</sup>, Aina E. Cohen<sup>h</sup>, James S. Fraser<sup>k</sup>, Michael E. Wall<sup>l</sup>, Henry van den Bedem<sup>d,k,1</sup>, and Mark A. Wilson<sup>a,1</sup>

<sup>a</sup>Department of Biochemistry and Redox Biology Center, University of Nebraska, Lincoln, NE 68588; <sup>b</sup>Chair of Applied Dynamics, Friedrich-Alexander University Erlangen-Nürnberg, 91058 Erlangen, Germany; <sup>c</sup>Bioengineering Department, Stanford University, Stanford, CA 94305; <sup>d</sup>Bioscience Division, SLAC National Accelerator Laboratory, Stanford University, Menlo Park, CA 94025; <sup>e</sup>Chemistry Department, University of Puerto Rico, Mayagüez PR 00681; <sup>f</sup>Lincac Coherent Light Source, SLAC National Accelerator Laboratory, Stanford University, Menlo Park, CA 94025; <sup>g</sup>Stanford PULSE Institute, SLAC National Accelerator Laboratory, Stanford University, Menlo Park, CA 94025; <sup>h</sup>Stanford Synchrotron Radiation Lightsource, SLAC National Accelerator Laboratory, Stanford University, Menlo Park, CA 94025; <sup>i</sup>Molecular Biophysics and Integrated Bioimaging Division, Lawrence Berkeley National Laboratory, Berkeley, CA 94720; <sup>j</sup>Department of Chemistry, University of Nebraska, Lincoln, NE 68588; <sup>k</sup>Department of Bioengineering and Therapeutic Sciences, California Institute for Quantitative Biology, University of California, San Francisco, CA 94158; and <sup>l</sup>Computer, Computational, and Statistical Sciences Division, Los Alamos National Laboratory, Los Alamos, NM 87505

Edited by Nigel S. Scrutton, The University of Manchester, Manchester, United Kingdom, and accepted by Editorial Board Member Stephen J. Benkovic November 6, 2019 (received for review January 31, 2019)

**How changes in enzyme structure and dynamics facilitate passage along the reaction coordinate is a fundamental unanswered question.** Here, we use time-resolved mix-and-inject serial crystallography (MISC) at an X-ray free electron laser (XFEL), ambient-temperature X-ray crystallography, computer simulations, and enzyme kinetics to characterize how covalent catalysis modulates isocyanide hydratase (ICH) conformational dynamics throughout its catalytic cycle. We visualize this previously hypothetical reaction mechanism, directly observing formation of a thioimidate covalent intermediate in ICH microcrystals during catalysis. ICH exhibits a concerted helical displacement upon active-site cysteine modification that is gated by changes in hydrogen bond strength between the cysteine thiolate and the backbone amide of the highly strained Ile152 residue. These catalysis-activated motions permit water entry into the ICH active site for intermediate hydrolysis. Mutations at a Gly residue (Gly150) that modulate helical mobility reduce ICH catalytic turnover and alter its pre-steady-state kinetic behavior, establishing that helical mobility is important for ICH catalytic efficiency. These results demonstrate that MISC can capture otherwise elusive aspects of enzyme mechanism and dynamics in microcrystalline samples, resolving long-standing questions about the connection between nonequilibrium protein motions and enzyme catalysis.

X-ray crystallography | cysteine modification | enzyme conformational dynamics | XFEL | radiation damage

Protein dynamics plays an important role in enzyme catalysis (1–4). Many enzymes form covalent catalytic intermediates that can alter enzyme structure and conformational dynamics (5–8). Because catalytic intermediates transiently modify enzymes, they may activate a new protein motion regime that facilitates later steps of catalysis. Determining how these transient changes in enzyme structure and dynamics facilitate passage along the reaction coordinate is a topic of intense interest in structural enzymology (4, 8). Of all amino acids in proteins, reactive cysteine residues are subject to the most diverse set of covalent modifications (9, 10). Moreover, the targeted modification of cysteine residues proximal to active sites has become a frontline strategy for the development of covalent enzyme inactivators as tools for chemical biology and drugs (11). Therefore, understanding how the H-bonding environment of active-site cysteine residues modulates their reactivity and how the covalent modification of cysteine thiolate anions controls protein conformational dynamics can provide general insights into the functions of many proteins whose activities require or are regulated by covalent modifications.

X-ray crystallography provides an atomically detailed ensemble- and time-averaged view of protein conformational dynamics in the lattice environment (12–15). Technological advances in X-ray sources, detectors, and sample delivery have enabled a new class of crystallography experiments that report on nonequilibrium protein motions in response to external perturbations (16). Because these perturbations can be selected for functional relevance (e.g., by the infusion of substrate or induction of a particular modification), the resulting nonequilibrium changes often correspond to functionally important protein motions. In parallel, advances in

## Significance

**Protein structures fluctuate owing to thermal motion and in response to functional changes such as ligand binding. As a consequence, it is challenging to determine which protein motions are functionally most important at equilibrium. Enzymes that are transiently covalently modified during catalysis offer a way to identify functional motions, as the modification can trigger catalytically important conformational changes. The covalent modification of the active-site cysteine in isocyanide hydratase weakens a critical hydrogen bond required for reactivity. Hydrogen bond disruption triggers a cascade of conformational changes whose modulation by mutation is detrimental to enzyme turnover. Most enzymes that form catalytic intermediates will experience similar transient changes in active-site electrostatics, suggesting that modification-gated conformational dynamics is common in enzymes.**

Author contributions: H.v.d.B. and M.A.W. designed research; M.D., D.B., S.H.P.D.O., P.M., D.M.-R., J.S., B.H., R.G.S., S.B., M.S.H., R.A.-M., A.B., J.W., A.L., A.S.B., N.K.S., G.A.A., V.K.T., D.B.B., M.C.T., A.E.C., J.S.F., M.E.W., H.v.d.B., and M.A.W. performed research; D.B., R.G.S., S.B., A.S.B., N.K.S., G.A.A., V.K.T., D.B.B., and H.v.d.B. contributed new reagents/analytic tools; J.W., M.E.W., H.v.d.B., and M.A.W. analyzed data; and M.D., J.S.F., H.v.d.B., and M.A.W. wrote the paper.

The authors declare no competing interest.

This article is a PNAS Direct Submission. N.S.S. is a guest editor invited by the Editorial Board.

Published under the [PNAS license](#).

Data deposition: Refined atomic coordinates and X-ray crystallographic data have been deposited in the RCSB Protein Data Bank, <http://www.rcsb.org> (accession nos. 6N14–6N19, 6N1A, 6NPQ, 6UND, and 6UNF).

<sup>1</sup>To whom correspondence may be addressed. Email: vdbedem@stanford.edu or mwilson13@unl.edu.

This article contains supporting information online at <https://www.pnas.org/lookup/suppl/doi:10.1073/pnas.1901864116/DCSupplemental>.

First published December 4, 2019.

computer modeling of multiple conformational substates now enable visualizing minor populations of crystalline protein structural ensembles. These approaches have permitted identification of networks of side-chain disorder (17), allowed refinement of whole-protein ensemble models (18), aided identification of minor binding modes of therapeutic ligands (19), and characterized spatial correlations in protein mobility (20).

The enzyme studied here is isocyanide hydratase (ICH; EC 4.2.1.103), a homodimeric cysteine-dependent enzyme in the DJ-1 superfamily that irreversibly hydrates many isocyanides to yield N-formamides (21) (Fig. 1A). Prior crystallographic studies of ICH showed evidence of helical mobility near the active-site Cys101 residue (Fig. 1A), which coincided with photooxidation of C101 to Cys101-SOH (22). Cys101 accepts an S<sup>-</sup>-HN hydrogen bond from the severely strained ( $\phi = 14^\circ$ ,  $\psi = -83^\circ$ ) backbone amide of Ile152. When this hydrogen bond is disrupted in an engineered C101A mutant (Fig. 1A), Ile152 relaxes to an unstrained backbone conformation concomitant with displacement of the helix (22, 23). The relevance of these motions for ICH function was not established in these prior studies.

Here, we use X-ray crystallography, molecular dynamics simulation, rigidity theory, mutagenesis, and enzyme kinetics to characterize a set of correlated conformational changes that remodel the ICH active site and propagate across the dimer interface

in response to cysteine modification. Using time-resolved mix-and-inject serial crystallography (MISC) at an X-ray free electron laser (XFEL), we directly observed formation of a covalent intermediate and transient, functionally important motions during ICH catalysis. Pre-steady-state kinetics of wild-type and mutant ICH suggests that cysteine-gated conformational changes are important for water to access and hydrolyze the catalytic intermediate. The prominence of conformational dynamics in ICH and the tractability of this protein using multiple biophysical techniques make ICH a valuable model system for understanding how cysteine modification can modulate functional protein dynamics.

## Results

**Structural Characterization of a Thioimide Intermediate and Helix Motion during ICH Catalysis.** We examined the role of active-site structural dynamics in ICH turnover by directly monitoring catalysis in ICH microcrystals using MISC at the Linac Coherent Light Source (LCLS) XFEL at 298 K. We infused the substrate p-nitrophenyl isocyanide (p-NPIC; *SI Appendix*) into a stream of unmodified ICH microcrystals (*Materials and Methods*) and collected diffraction data at carefully selected time delays (*SI Appendix*, Fig. S1). The concentration of p-NPIC in the stream allowed only a single turnover of crystalline ICH before substrate depletion. The proposed reaction mechanism for ICH postulates

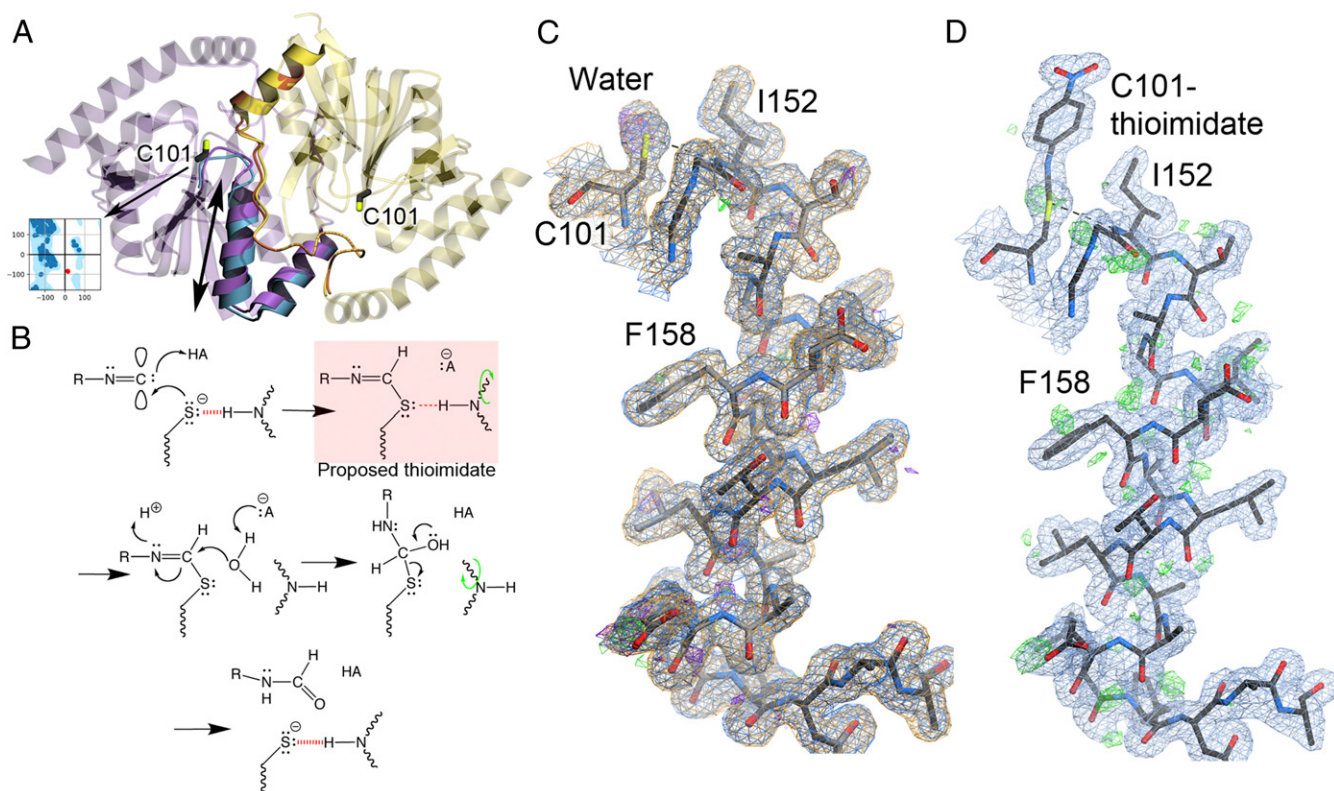


**Fig. 1.** Catalytic intermediate captured with MISC. (A) The ICH dimer is shown as an overlay of WT ICH (purple) and C101A ICH (blue). The “B” protomer is shown in yellow. The mobile helix H in C101A and areas exhibiting correlated backbone–side-chain disorder are rendered opaque. Ile152 is a Ramachandran outlier (*Inset*) whose backbone torsion angles move with helical displacement. (B) Postulated reaction mechanism for ICH, beginning with Cys101 thiolate attack at the electrophilic carbene carbon atom of isocyanide substrates and proceeding in the direction of the arrows. A previously postulated thioimide intermediate (red box) eliminates the charge on Cys101 and weakens the H-bond to Ile152 (dashed red line). This relieves backbone torsional strain at Ile152 and permits sampling of shifted helix H conformations (green curved arrow), allowing water access to the intermediate for hydrolysis. (C) ICH completes a full catalytic cycle in the crystal during MISC. Helix H is shown with 2mF<sub>o</sub>-DF<sub>c</sub> electron density (0.8 rmsd) prior to the introduction of substrate (blue) and after substrate has been exhausted (orange). These maps overlap almost perfectly, indicating that ICH is fully restored to its resting conformation after catalysis. The hydrogen bond between the peptide backbone of Ile152 and Cys101 is shown in a dotted line. The helix is not mobile in these resting structures, indicated by the absence of features in the mF<sub>o</sub>-DF<sub>c</sub> difference electron density (2.5 rmsd prior to substrate [green] and after catalysis is complete [purple]) (D) MISC confirms that ICH forms a covalent Cys101-thioimide intermediate 15 s after substrate mixing. Difference mF<sub>o</sub>-DF<sub>c</sub> electron density contoured at 2.5 rmsd (green) supports sampling of shifted helix H conformations upon intermediate formation.

that the catalytic Cys101 nucleophile attacks organic isocyanides at the electron-deficient carbene-like center, followed by proton abstraction from a nearby general acid to generate a covalent thioimidate intermediate (Fig. 1*B*). An enzyme-linked thioimidate, which has not been previously observed, eliminates the negative charge of the Cys101 thiolate ( $S^-$ ) and is proposed to reduce the strength of the Cys101-Ile152 hydrogen bond. Because the “diffraction before destruction” principle ensures that serial XFEL diffraction data are minimally affected by X-ray radiation damage (24), the enzyme suffered no radiation-induced oxidation of Cys101 (Fig. 1*C*). After 15 s of mixing, 2mF<sub>o</sub>-DF<sub>c</sub> (Fig. 1*D*) and omit mF<sub>o</sub>-DF<sub>c</sub> electron density maps (*SI Appendix*, Fig. S2*A*) unambiguously revealed the formation of a thioimidate covalent intermediate in both ICH protomers. Once the intermediate is formed, positive mF<sub>o</sub>-DF<sub>c</sub> difference electron density appears around helix H (Fig. 1*D*) and its B-factors increase (*SI Appendix*, Fig. S2*B–D*), indicating that it samples a new conformational ensemble. This difference density and the elevated B-factors are absent both prior to catalysis and after ICH has exhausted substrate 5 min after mixing (Fig. 1*C* and *SI Appendix*, Fig. S2*B–D*). Therefore, helix H becomes trans-

siently mobile upon intermediate formation during ICH catalysis, dynamically changing the active-site microenvironment.

**Cys101 Modification Triggers Conformational Changes that Remodel the ICH Active Site.** We reasoned that the on-pathway thioimidate intermediate weakens the Cys101-Ile152 hydrogen bond that holds helix H in a strained conformation similarly to the X-ray-induced Cys101-SOH modification in the resting enzyme (22). Consistent with this idea, the cryogenic dataset collected at 100 K (Cryo) showed evidence of radiation-driven Cys101-SOH formation and a corresponding increase in helical mobility (Fig. 2*A*) (22). To enrich populations of the shifted conformation, we therefore collected a series of X-ray diffraction datasets of wild-type (WT) ICH at increasing absorbed doses of X-ray radiation (Fig. 2 *A–C*). Two ambient-temperature (274–277 K) synchrotron radiation datasets at 1.20–1.15 Å revealed radiation-dose-dependent Cys101 oxidation and helical displacement with increasing occupancy (Fig. 2*D*). Refined occupancies of alternate conformations of helix H confirmed a population shift toward the displaced helix position along this series of datasets that correlates with the extent of absorbed X-ray dose and concomitant

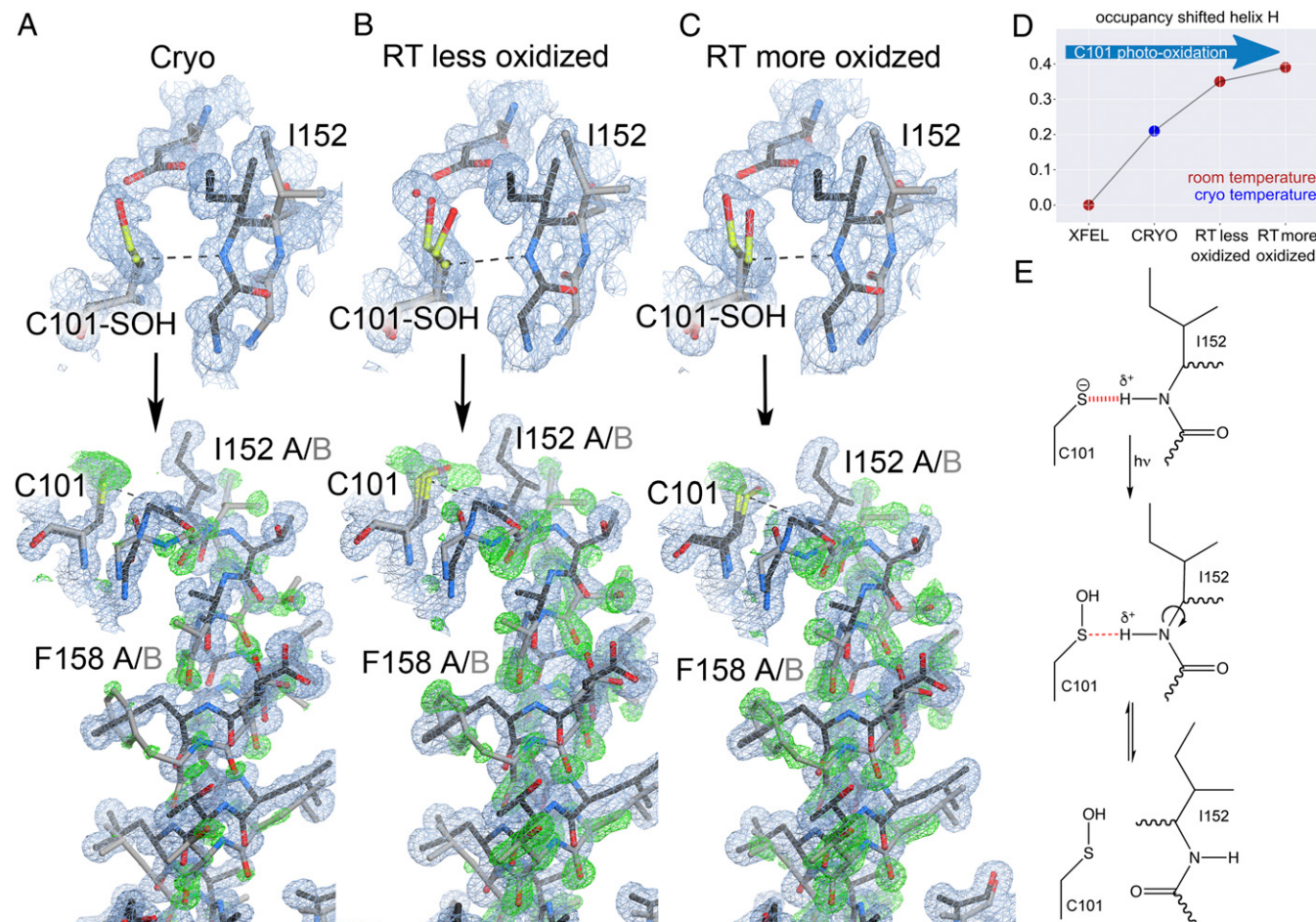


**Fig. 2.** X-ray-induced cysteine oxidation drives helical motion in ICH. (*A–C, Upper*) The environment of Cys101 with varying degrees of oxidation to Cys101-sulfenic acid. 2mF<sub>o</sub>-DF<sub>c</sub> electron density is contoured at 0.7 rmsd (blue), and the hydrogen bond between the peptide backbone of Ile152 and Cys101 is shown in a dotted line. “Cryo” is synchrotron data collected at 100 K (PDB 3NON); “RT less oxidized” is synchrotron data collected at 274 K with an absorbed dose of  $2.4 \times 10^4$  Gy; and “RT more oxidized” is synchrotron data collected at 277 K with an absorbed dose of  $3.7 \times 10^5$  Gy. (*Lower*) helix H in its strained (black) and relaxed, shifted conformations (gray). 2mF<sub>o</sub>-DF<sub>c</sub> electron density is contoured at 0.8 rmsd (blue) and omit mF<sub>o</sub>-DF<sub>c</sub> electron density for the shifted helical conformation is contoured at 3.0 rmsd (green). At 274–277 K, increased Cys101 oxidation disrupts the hydrogen bond to Ile152 and results in stronger difference electron density for the shifted helix conformation. (*D*) The refined occupancy of helix H in each X-ray dataset indicates that increases in temperature and Cys101 oxidation result in higher occupancy for the shifted (relaxed) helix conformation. (*E*) Mechanism of X-ray-induced covalent modification of C101 and weakening of the S-HN hydrogen bond.

Cys101 oxidation. The shifted helix conformations across datasets are highly similar, suggesting that the observed electron density features resulted from coupling between this helix and specific, radiation-induced photochemistry at Cys101.

Notably, these stronger density peaks correspond to the difference electron density observed in the MISC experiment during ICH catalysis (Figs. 1D and 2A–C). In the ambient-temperature synchrotron radiation datasets, the helical shift is caused by radiation-induced oxidation of Cys101, which eliminates the negative charge on the Sy thiolate ( $\text{Cys101-S}^-$ ) and thus weakens the hydrogen bond between the amide H of Ile152 and Cys101-S $^-$ . This hydrogen bond goes from  $-2.2 \text{ kcal/mol}$  with a Cys101-S $^-$  acceptor to  $-0.91 \text{ kcal/mol}$  with a Cys101-SOH acceptor (Fig. 2E and *SI Appendix*, Fig. S3). Similar loss of Cys101 thiolate negative charge occurs during formation of the on-pathway thioimidate intermediate, which also weakens the Cys101-Ile152 hydrogen bond (Fig. 1B).

#### Molecular Dynamics Simulations Support a Thiolate-Hydrogen Bond Restraint Mechanism.

To investigate the local dynamical response of ICH to cysteine modification, we used molecular dynamics (MD) simulations of the reduced (Cys101-S $^-$ ) and Cys101-SOH crystals of ICH. We simulated the Cys101-SOH adduct rather than the thioimidate catalytic intermediate because it reports on the effects of charge neutralization (Fig. 2E and *SI Appendix*, Fig. S3) more directly without the structural effects of the larger bound thioimidate intermediate or biases from thioimidate parameterization. Simulations of Cys101-S $^-$  were started from the XFEL crystal structure (“XFEL” simulation, Fig. 3A and B, red) while the Cys101-SOH-oxidized structure was similar to the synchrotron radiation (SR-) oxidized structure (“SR” simulation, Fig. 3A and B, blue). For the XFEL simulation, the Ile152-Cys101-S $^-$

hydrogen bond was predominantly maintained in the simulated crystal for the full 1- $\mu\text{s}$  length of the MD trajectory ( $d_{\text{avg}}(\text{C101}_{\text{SG}}, \text{I152}_H) = 2.8 \text{ \AA}$ ; Fig. 3A). By contrast, in simulations of the SR Cys101-SOH state the hydrogen bond typically dissociated very early in the trajectory ( $d_{\text{avg}}(\text{C101}_{\text{SG}}, \text{I152}_H) = 4.3 \text{ \AA}$ ; Fig. 3A). Moreover, several protomers in the simulated Cys101-SOH crystal experienced a shift of helix H similar to that observed in the ambient-temperature synchrotron radiation datasets (mean shift  $0.69 \text{ \AA}$ ; Fig. 3B and *Movie S1*). These helical shifts were observed less frequently in simulations with the Cys101-S $^-$  (mean shift  $0.60 \text{ \AA}$ ; Fig. 3B), consistent with the hypothesis that local redistribution of cysteine electrostatic charge modulates these long-range motions.

**Widespread Dynamic Conformational Responses to Cysteine Modification in ICH.** Root-mean-square fluctuations (rmsfs) calculated along a simulation trajectory show widespread movement across the entire dimer (Fig. 3C). Consistent with this simulation result, an  $F_o(\text{SR}) - F_o(\text{XFEL}_{\text{FREE}})$  isomorphous difference electron density map of the Cys101-SOH SR dataset ( $F_o(\text{SR})$ ) and the Cys101-S $^-$  XFEL dataset of the free enzyme before substrate was introduced ( $F_o(\text{XFEL}_{\text{FREE}})$ ) reveal widely distributed difference features (Fig. 3D). A difference map calculated between the 15-s thioimidate intermediate XFEL dataset and the free-enzyme XFEL dataset ( $F_o(\text{XFEL}_{15s}) - F_o(\text{XFEL}_{\text{FREE}})$ ) shows overlapping but weaker features, confirming that formation of the thioimidate intermediate during ICH catalysis shifts the conformational ensemble similarly to cysteine oxidation (*SI Appendix*, Fig. S4). The  $F_o(\text{SR}) - F_o(\text{XFEL}_{\text{FREE}})$  difference map features are most prominent in protomer A near the active site and the mobile helix H (Fig. 3D). Difference features at the active site correspond to the dramatic conformational change of a conserved diglycyl motif,

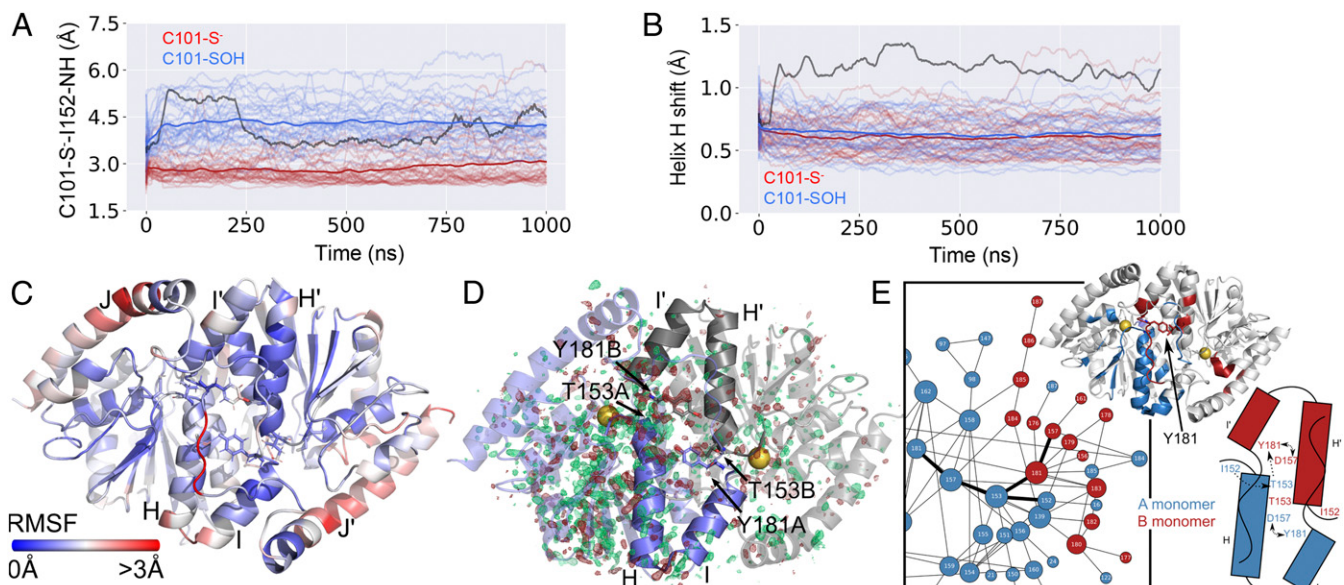


**Fig. 3.** Cysteine modification results in a protein-wide conformational response. (A) Fluctuations of the  $\text{C101}_{\text{SG}}-\text{I152}_H$  distance in simulations of ICH crystals in the Cys101-S $^-$  (red) or Cys101-SOH (blue) state. Each ICH dimer is represented by a semitransparent line. Opaque red and blue lines denote the average  $\text{C101}_{\text{SG}}-\text{I152}_H$  distance across the dimers. (B) Conformational shift of helix H in the Cys101-S $^-$  (red) or Cys101-SOH (blue) state. The dark gray lines in A and B represent the trajectory selected for *Movie S1*. (C) rmsfs calculated from MD simulations indicate highest fluctuations in linker I'-J' of the B protomer. Helix H of the A protomer just underneath the linker also shows elevated rmsfs. (D) An isomorphous  $F_o(\text{SR}) - F_o(\text{XFEL}_{\text{FREE}})$  difference map reveals features (green, positive; red, negative) distributed throughout the dimer, suggesting broadly altered structure and dynamics upon formation of the Cys101-SOH in the 274-K synchrotron radiation ( $F_o(\text{ORT})$ ) dataset. The “A” conformer is shown in slate blue, and the “B” conformer is shown as a gray semitransparent cartoon. Helices H and I are opaque in both conformers. The catalytic nucleophile is shown in spheres. Difference electron density features are nonuniformly distributed, with stronger features near helix H in the A protomer, and along region B169–B189, which contacts the N-terminal end of helix H. Maps are contoured at  $\pm 3.0 \text{ rmsd}$ . (E) CONTACT analysis identifies allosteric coupling across the dimer interface, in striking agreement with isomorphous difference maps and rmsfs from D. The A protomer is color-coded in blue; the B protomer, in red. Residues identified in the CONTACT analysis are projected onto the cartoon.

G150-G151 and Ile152, while those near the interface of helix H and the  $\beta$ -sheet in protomer A reflect residues adjusting their position in response to helix H motion. There are far fewer peaks in protomer B, consistent with the absence of mobility of helix H' in that protomer. However, the  $F_0$ (SR) –  $F_0$ (XFEL<sub>FREE</sub>) map reveals significant features along the C terminus of helix I' at the dimer interface in protomer B, which directly contacts ThrA153 through TyrB181 (Fig. 3D). These peaks likely report on conformational changes allosterically propagating from protomer A through the I'J' linker (residues 181–185, where primes indicate that the linker is contributed by protomer B) into protomer B. By contrast, the difference map around the C terminus of helix I and linker IJ in protomer A (IJ<sub>A</sub>, which packs against the stationary helix H of protomer B) is comparatively featureless.

Notably, the simulations indicate that the conformational shift in linker I'J' toward the unshifted helix H' is larger than observed in the crystal structure (Movie S1). Our simulations suggest that the I'J' conformational shift can precede relaxation of the strained Ile152 conformation and subsequent shift of helix H by several nanoseconds, allosterically communicating dynamical changes in protomer A across the dimer interface into protomer B, reminiscent of interprotomer communication observed in other systems (4). We further examined dynamical communication across the dimer interface in ICH using CONTACT (contact networks through alternate conformation transitions) network analysis of the electron density maps. CONTACT elucidates pathways of collective amino acid main- and side-chain displacements by mapping van der Waals conflicts in multiconformer qFit models (25) that would result from side-chain conformational disorder if correlated motions were not considered (17). CONTACT identified a large network of correlated residues in protomer A (with the mobile helix) that connects with a smaller network in protomer B (Fig. 3E), corroborating the isomorphous difference maps. We then used rigidity analysis (SI Appendix, Fig. S5) and

kinematic flexibility analysis (KFA; ref. 26) to analyze how the Cys101-Ile152 hydrogen bond modulates motion modes accessible to the enzyme (SI Appendix, Fig. S6). Using KFA, we compared motion modes corresponding to the lowest mode-specific free energies in the XFEL structure when the H-bond is intact in both A and B protomers (C101-I152<sub>A&B</sub>) to those present when this H-bond is disrupted in protomer A (C101-I152<sub>B</sub>) (SI Appendix, Fig. S6). These altered motion modes are those most sensitive to disruption of the hydrogen bond. Perturbations in the hydrogen-bonding network are propagated primarily to the IJ linkers, helices H and I and helices J and J', consistent with the MD simulations. Strikingly, KFA predicted large rmsfs within the IJ<sub>A</sub> linker near the active site in protomer B, suggesting that the two sites are in allosteric communication. Considered together, the isomorphous difference electron density map, CONTACT analysis, KFA, and long-time MD simulations indicate that catalytically important local changes in hydrogen bonding at Cys101 initiate a cascade of dynamical changes that propagate across the entire ICH dimer in an asymmetric manner (4).

#### Cysteine Modification–Gated Motions Increase ICH Catalytic Efficiency.

To modulate helical mobility and measure the impact on ICH catalysis, we designed two mutations, G150A and G150T. G150 is part of a highly conserved diglycyl motif that moves ~3 Å to accommodate helical motion in ICH. Ambient-temperature (274–277 K) crystal structures of G150A and G150T ICH show that the added steric bulk at this position biases the helix toward its relaxed conformation (Fig. 4 A and B). In G150A ICH, helix H samples both conformations in both protomers whereas only one protomer of WT ICH shows helical motion (Fig. 4A and SI Appendix, Fig. S7). By contrast, the G150T structure shows helix H constitutively shifted to its relaxed position (Fig. 4B). Both G150A and G150T have an alternate Cys101 side-chain conformation which conflicts with the unshifted conformation of Ile152 and helix H (Fig. 4 A

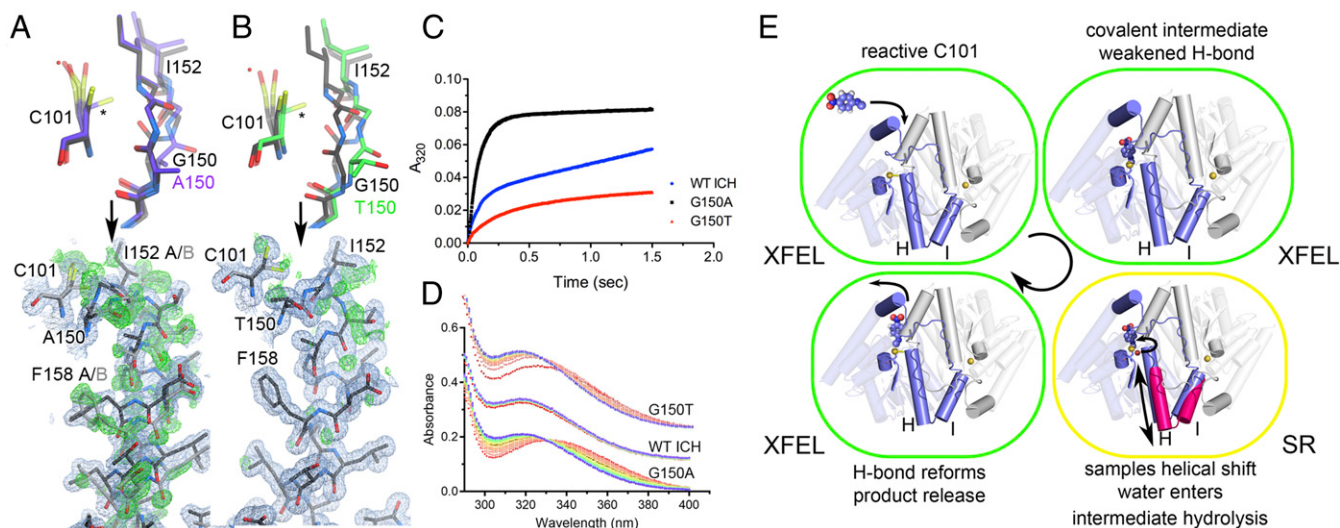


**Fig. 4.** Mutations at Glu150 alter helical mobility and reduce ICH catalytic turnover. (A and B) The environment of Cys101 in Gly150A and G150T ICH (Top). 2mF<sub>o</sub>-DF<sub>c</sub> electron density is contoured at 0.7 rmsd (blue) and the hydrogen bond appears as a dotted line. Both G150 mutations permit unmodified Cys101 to sample conformations (asterisk) that sterically conflict with Ile152 in the strained helical conformation (black), requiring the helix to sample shifted conformations (gray) in the absence of Cys101 modification. (A and B, Lower) The helix in its strained (black) and relaxed, shifted conformations (gray). 2mF<sub>o</sub>-DF<sub>c</sub> electron density is contoured at 0.8 rmsd (blue) and omit mF<sub>o</sub>-DF<sub>c</sub> electron density is contoured at +3.0 rmsd (green). (C) Pre-steady-state enzyme kinetics of WT (blue circles), G150A (black squares), and G150T (red triangles) ICH at 160  $\mu$ M p-NPIC shows a pronounced burst phase for each protein with differing burst and steady-state rate constants. The divergent pre-steady-state profiles indicate that G150A impacts steps after the first chemical step, while G150T affects both early and later steps. (D) Single-turnover spectra of ICH enzymes with p-NPIC substrate shown from early (red) to later (blue) timepoints in 5-s increments. At early times, G150A and G150T accumulate a species with  $\lambda_{\text{max}} = 335$  nm, likely the thioimidate intermediate that resolves to product in the blue spectra with  $\lambda_{\text{max}} = 320$  nm. (E) The catalytic cycle of ICH. Substrate binds with Cys101-S<sup>–</sup> poised for nucleophilic attack and with the Cys101-Ile152 H-bond intact. Formation of the thioimidate intermediate weakens the Cys101-Ile152 H-bond and causes helical motion (magenta helices H and I) that promotes intermediate hydrolysis (red sphere; curved arrow). Hydrolysis of the thioimidate intermediate restores the reactive C101-S<sup>–</sup> and strengthens the Cys101-Ile152 H-bond, favoring the strained helical conformation.

and *B*, asterisk), indicating that the helix must move partially independently of Cys101 modification in these mutants. As in wild-type ICH, G150A shows evidence of Cys101-SOH oxidation in the electron density (Fig. 4*A*). By contrast, Cys101 in G150T ICH is not modified by comparable exposure to X-rays (Fig. 4*B*), indicating that the Ile152-NH-Cys101-S<sup>−</sup> hydrogen bond is important for enhancing Cys101 reactivity.

Unlike the C101A mutant, which shows similar helical displacement but is catalytically inactive, G150A and G150T ICH are catalytically active. This allowed us to investigate the role of helical displacement in the ICH catalytic cycle. Steady-state enzyme kinetics of the G150A and G150T mutants measured using p-NPIC as the substrate showed a ~6-fold reduction in  $k_{cat}$  for both mutants compared to the wild-type enzyme but largely unchanged  $K_m$  values (*SI Appendix Fig. S8 and Table S1*). In contrast to their similar steady-state kinetic behavior, the G150 mutants have divergent pre-steady-state kinetic profiles in stopped-flow mixing. ICH exhibits “burst” kinetics (Fig. 4*C*), indicating that the rate-limiting step for ICH catalysis comes after formation of the thioimidate intermediate. G150A ICH has a burst exponential rate constant  $k$  of  $\sim 11\text{ s}^{-1}$  that is comparable to the wild-type enzyme, but G150T has a reduced burst rate constant of  $\sim 4\text{ s}^{-1}$ , indicating a slower chemical step (Fig. 4*C* and *SI Appendix, Fig. S8 and Table S1*). WT and G150A ICH have comparable second-order rate constants for the burst phase, while G150T is markedly slower (*SI Appendix, Fig. S8 and Table S1*). In addition, the burst amplitude of G150A is approximately twice as large as that of the wild-type ICH despite equal concentrations of enzyme (Fig. 4*C*), which correlates with both protomers of G150A having a mobile helix H compared to only one protomer of wild-type ICH (*SI Appendix, Fig. S7*). This suggests communication between the two active sites in the ICH dimer that is dynamically gated by helix H.

Although both the G150A and G150T mutations impair ICH catalysis, the kinetic effect of the G150A mutation is predominantly in steps after formation of the intermediate, while G150T impairs both the rate of intermediate formation and, later, the rate-limiting steps. Furthermore, we observed spectral evidence for the thioimidate intermediate in single-turnover UV-visible spectra (Fig. 4*D*). G150A ICH accumulates a species whose absorbance maximum is 335 nm, while WT ICH completes a single turnover and accumulates the 320-nm formamide product in the  $\sim 30\text{-s}$  deadtime of manual mixing (Fig. 4*D*). G150T ICH accumulates less of the 335-nm intermediate than G150A ICH due to a closer match between the rates of formation and consumption of the intermediate in G150T ICH. In G150A ICH, the 335-nm species slowly converts to the 320-nm product over  $\sim 40\text{ s}$  (Fig. 4*D*), consistent with the slow rate of product formation observed after the burst in G150A pre-steady-state kinetics (Fig. 4*C*). These data support the conclusion that the 335-nm species is the ICH-thioimidate intermediate observed in the MISC experiment and that G150A is impaired in hydrolyzing this covalent intermediate from the active-site Cys101 due to the perturbed dynamics of helix H.

## Discussion

Covalent modification is a common and physiologically important perturbation to proteins. Reactive residues such as cysteine are prone to diverse covalent modifications with catalytic or regulatory consequences. Moreover, cysteine residues are attractive targets for covalent inhibitors, which hold great promise for the generation of highly potent and selective drugs (11). We found that cysteine modification in ICH remodels active-site H-bonding networks and gates catalytically important changes in protein dynamics with a clearly defined mechanism. Modification of the active-site cysteine thiolate during catalysis neutralizes its negative charge and weakens a key H-bond, activating correlated motions that span the entire ICH dimer. Transiently increased flexibility of the active site facilitates water entry and

attack at the thioimidate to form a proposed tetrahedral intermediate. The H-bond between Cys101 and Ile152 then reforms, stabilizing the nascent Cys101 thiolate and making it a better leaving group, thereby coupling dynamical changes in the enzyme to progress along the reaction coordinate (Fig. 4*E*). Notably, all cysteine thiolates experience a similar loss of negative charge upon covalent bond formation. Because cysteine residues can have multiple roles in a protein, including catalytic nucleophile, metal ligand, acylation target, redox target, covalent inhibitor target, and others, many different modification-mediated signals may be transduced through altered cysteine electrostatics to impact protein dynamics and function, expanding the ways in which cysteine can couple protein biophysical properties to cellular needs. Integrating recent developments in serial and conventional room-temperature (RT) crystallography with advanced computational methods (27) can offer exciting opportunities to reveal enzyme mechanisms and interrogate the consequences of cysteine modification for protein dynamics.

## Materials and Methods

*Pseudomonas fluorescens* ICH was expressed in *E. coli* as a thrombin-cleavable, N-terminally 6xHis-tagged protein and purified as previously described (22). Crystals in space group P2<sub>1</sub> were grown using hanging drop vapor equilibration for synchrotron datasets and by batch microseeding for the XFEL data collections. Synchrotron data were collected at the Stanford Synchrotron Radiation Laboratory (SSRL) from capillary-mounted crystals at 274–277 K. XFEL data were collected at the Macromolecular Femtosecond Crystallography (MFX) end station at the LCLS at 298 K. Models were fitted into electron density maps in COOT (28) and refined in PHENIX (29). Crystallographic data and model statistics are provided in the *SI Appendix, Tables S2 and S3*. Molecular dynamics simulations were performed using the Schrödinger 2018–3 software suite. Steady-state and pre-steady-state enzyme kinetics was measured for recombinant ICH proteins using the model substrate p-NPIC, and formamide product formation was monitored by absorption at 320 nm. Detailed methods are provided in the *SI Appendix*.

**Data Availability.** All coordinates and structure factors are freely available for download from the RCSB Protein Data Bank (<http://www.rcsb.org>).

**ACKNOWLEDGMENTS.** We thank Dr. Donald Becker (University of Nebraska) and Dr. Joseph Barycki (North Carolina State University) for helpful discussions and Lauren Barbee (University of Nebraska) for assistance with ICH kinetic data and analysis. R.G.S. acknowledges the support of the Office of Basic Energy Sciences through the Atomic, Molecular, and Optical Sciences Program program within the Chemical Sciences, Geosciences, and Biosciences Division and of the US Department of Energy (DOE) through the SLAC Laboratory Directed Research and Development Program. A.S.B. and N.K.S. were supported by National Institutes of Health (NIH) grant GM117126 to N.K.S. for data-processing methods. M.C.T. and J.S.F. were supported by the National Science Foundation (NSF) (STC-1231306), by a Ruth L. Kirschstein National Research Service Award (F32 HL129989) to M.C.T., and by awards to J.S.F. from the NIH (GM123159, GM124149), the David and Lucile Packard Foundation (Packard Fellowship), and the University of California (UC) Office of the President Laboratory Fees Research Program (LFR-17-476732). M.E.W. was supported by the Exascale Computing Project (17-SC-20-SC), a collaborative effort of the DOE, Office of Science, and the National Nuclear Security Administration, and the UC Office of the President Laboratory Fees Research Program (LFR-17-476732). S.H.P.D.O. and H.v.d.B. are supported by award NIH GM123159 to H.v.d.B. H.v.d.B. is supported by a Mercator Fellowship from the Deutsche Forschungsgemeinschaft (DFG). M.A.W. was supported by the Nebraska Tobacco Settlement Biomedical Research Development Fund. Use of the SSRL, SLAC National Accelerator Laboratory, is supported by the DOE, Office of Science, Office of Basic Energy Sciences, under Contract No. DE-AC02-76SF00515. The SSRL Structural Molecular Biology Program is supported by the DOE, Office of Biological and Environmental Research, and by the NIH, National Institute of General Medical Sciences (NIGMS) (including P41GM103393). Use of the LCLS, SLAC National Accelerator Laboratory, is supported by the DOE, Office of Science, Office of Basic Energy Sciences, under Contract No. DE-AC02-76SF00515. The helium-rich ambient system for in-helium experiments at MFX was developed by Bruce Doak and funded by the Max Planck Institute for Medical Research. This research used resources of the Advanced Photon Source, a DOE, Office of Science, User Facility operated for the DOE, Office of Science, by Argonne National Laboratory under Contract No. DE-AC02-06CH11357. Use of BioCARS was also supported by NIH NIGMS under grant number R24GM111072. The contents of this publication are solely the responsibility of the authors and do not necessarily represent the official views of NIGMS or NIH.

1. K. Danyal, D. Mayweather, D. R. Dean, L. C. Seefeldt, B. M. Hoffman, Conformational gating of electron transfer from the nitrogenase Fe protein to MoFe protein. *J. Am. Chem. Soc.* **132**, 6894–6895 (2010).
2. K. A. Henzler-Wildman *et al.*, Intrinsic motions along an enzymatic reaction trajectory. *Nature* **450**, 838–844 (2007).
3. H. Y. Aviram *et al.*, Direct observation of ultrafast large-scale dynamics of an enzyme under turnover conditions. *Proc. Natl. Acad. Sci. U.S.A.* **115**, 3243–3248 (2018).
4. T. H. Kim *et al.*, The role of dimer asymmetry and protomer dynamics in enzyme catalysis. *Science* **355**, eaag2355 (2017).
5. G. G. Hammes, Multiple conformational changes in enzyme catalysis. *Biochemistry* **41**, 8221–8228 (2002).
6. S. Kale *et al.*, Efficient coupling of catalysis and dynamics in the E1 component of Escherichia coli pyruvate dehydrogenase multienzyme complex. *Proc. Natl. Acad. Sci. U.S.A.* **105**, 1158–1163 (2008).
7. P. Mehrabi *et al.*, Time-resolved crystallography reveals allosteric communication aligned with molecular breathing. *Science* **365**, 1167–1170 (2019).
8. K. M. Stiers *et al.*, Structural and dynamical description of the enzymatic reaction of a phosphohexomutase. *Struct. Dyn.* **6**, 024703 (2019).
9. N. J. Pace, E. Weerapana, Diverse functional roles of reactive cysteines. *ACS Chem. Biol.* **8**, 283–296 (2013).
10. K. G. Reddie, K. S. Carroll, Expanding the functional diversity of proteins through cysteine oxidation. *Curr. Opin. Chem. Biol.* **12**, 746–754 (2008).
11. R. Lonsdale, R. A. Ward, Structure-based design of targeted covalent inhibitors. *Chem. Soc. Rev.* **47**, 3816–3830 (2018).
12. N. Furnham, T. L. Blundell, M. A. DePristo, T. C. Terwilliger, Is one solution good enough? *Nat. Struct. Mol. Biol.* **13**, 184–185 (2006).
13. J. S. Fraser *et al.*, Accessing protein conformational ensembles using room-temperature X-ray crystallography. *Proc. Natl. Acad. Sci. U.S.A.* **108**, 16247–16252 (2011).
14. J. L. Smith, W. A. Hendrickson, R. B. Honzatko, S. Sheriff, Structural heterogeneity in protein crystals. *Biochemistry* **25**, 5018–5027 (1986).
15. M. A. Wilson, A. T. Brunger, The 1.0 Å crystal structure of Ca(2+)-bound calmodulin: An analysis of disorder and implications for functionally relevant plasticity. *J. Mol. Biol.* **301**, 1237–1256 (2000).
16. J. M. Martin-Garcia, C. E. Conrad, J. Coe, S. Roy-Chowdhury, P. Fromme, Serial femtosecond crystallography: A revolution in structural biology. *Arch. Biochem. Biophys.* **602**, 32–47 (2016).
17. H. van den Bedem, G. Bhabha, K. Yang, P. E. Wright, J. S. Fraser, Automated identification of functional dynamic contact networks from X-ray crystallography. *Nat. Methods* **10**, 896–902 (2013).
18. B. T. Burnley, P. V. Afonine, P. D. Adams, P. Gros, Modelling dynamics in protein crystal structures by ensemble refinement. *eLife* **1**, e00311 (2012).
19. G. C. P. van Zundert, *et al.*, qFit-ligand reveals widespread conformational heterogeneity of drug-like molecules in X-ray electron density maps. *J. Med. Chem.* **61**, 11183–11198 (2018).
20. M. E. Wall, A. M. Wolff, J. S. Fraser, Bringing diffuse X-ray scattering into focus. *Curr. Opin. Struct. Biol.* **50**, 109–116 (2018).
21. M. Goda, Y. Hashimoto, S. Shimizu, M. Kobayashi, Discovery of a novel enzyme, isonitrile hydratase, involved in nitrogen-carbon triple bond cleavage. *J. Biol. Chem.* **276**, 23480–23485 (2001).
22. M. Lakshminarasimhan, P. Madzelan, R. Nan, N. M. Milkovic, M. A. Wilson, Evolution of new enzymatic function by structural modulation of cysteine reactivity in *Pseudomonas fluorescens* isocyanide hydratase. *J. Biol. Chem.* **285**, 29651–29661 (2010).
23. A. E. Brereton, P. A. Karplus, Native proteins trap high-energy transit conformations. *Sci. Adv.* **1**, e1501188 (2015).
24. H. N. Chapman, C. Caleman, N. Timneanu, Diffraction before destruction. *Philos. Trans. R. Soc. Lond. B Biol. Sci.* **369**, 20130313 (2014).
25. H. van den Bedem, A. Dhanik, J. C. Latombe, A. M. Deacon, Modeling discrete heterogeneity in X-ray diffraction data by fitting multi-conformers. *Acta Crystallogr. D Biol. Crystallogr.* **65**, 1107–1117 (2009).
26. D. Budday, S. Leyendecker, H. van den Bedem, Kinematic flexibility analysis: Hydrogen bonding patterns impart a spatial hierarchy of protein motion. *J. Chem. Inf. Model.* **58**, 2108–2122 (2018).
27. H. van den Bedem, J. S. Fraser, Integrative, dynamic structural biology at atomic resolution—It's about time. *Nat. Methods* **12**, 307–318 (2015).
28. P. Emsley, K. Cowtan, Coot: Model-building tools for molecular graphics. *Acta Crystallogr. D Biol. Crystallogr.* **60**, 2126–2132 (2004).
29. P. D. Adams *et al.*, PHENIX: A comprehensive Python-based system for macromolecular structure solution. *Acta Crystallogr. D Biol. Crystallogr.* **66**, 213–221 (2010).

## Supporting Information

### Mix-and-inject XFEL crystallography reveals gated conformational dynamics during enzyme catalysis

Medhanjali DasGupta<sup>1</sup>, Dominik Budday<sup>2</sup>, Saulo H.P. de Oliveira<sup>3,4</sup>, Peter Madzelan<sup>1</sup>, Darya Marchany-Rivera<sup>5</sup>, Javier Seravalli<sup>1</sup>, Brandon Hayes<sup>6</sup>, Raymond G. Sierra<sup>6,7</sup>, Sébastien Boutet<sup>6</sup>, Mark S. Hunter<sup>6</sup>, Roberto Alonso-Mori<sup>6</sup>, Alexander Batyuk<sup>6</sup>, Jennifer Wierman<sup>8</sup>, Artem Lyubimov<sup>8</sup>, Aaron S. Brewster<sup>9</sup>, Nicholas K. Sauter<sup>9</sup>, Gregory A. Applegate<sup>10</sup>, Virendra Tiwari<sup>10</sup>, David B. Berkowitz<sup>10</sup>, Michael C. Thompson<sup>11</sup>, Aina E. Cohen<sup>8</sup>, James S. Fraser<sup>11</sup>, Michael E. Wall<sup>12</sup>, Henry van den Bedem<sup>4,11\*</sup>, Mark A. Wilson<sup>1\*</sup>

\* co-corresponding authors: mwilson@unl.edu and vdbedem@stanford.edu

<sup>1</sup>Department of Biochemistry and the Redox Biology Center, University of Nebraska, Lincoln, NE 68588, USA.

<sup>2</sup>Chair of Applied Dynamics, Friedrich-Alexander University Erlangen-Nürnberg, 91058 Erlangen, Germany.

<sup>3</sup>Bioengineering Department, Stanford University, Stanford, CA 94305, USA.

<sup>4</sup>Bioscience Division, SLAC National Accelerator Laboratory, Stanford University, Menlo Park, CA 94025, USA.

<sup>5</sup>Chemistry Department, University of Puerto Rico Mayaguez, Mayagüez PR 00681, USA

<sup>6</sup>Linac Coherent Light Source, SLAC National Accelerator Laboratory, Stanford University, Menlo Park, CA 94025, USA.

<sup>7</sup>Stanford PULSE Institute, SLAC National Accelerator Laboratory, Stanford University, Menlo Park, CA 94025, USA.

<sup>8</sup>Stanford Synchrotron Radiation Lightsource, SLAC National Accelerator Laboratory, Stanford University, Menlo Park, CA 94025, USA.

<sup>9</sup>Lawrence Berkeley National Laboratory, Berkeley, CA 94720, USA.

<sup>10</sup>Department of Chemistry, University of Nebraska, Lincoln, NE 68588, USA.

<sup>11</sup>Department of Bioengineering and Therapeutic Sciences, California Institute for Quantitative Biology, University of California, San Francisco, San Francisco, CA 94158, USA.

<sup>12</sup>Computer, Computational, and Statistical Sciences Division, Los Alamos National Laboratory, Los Alamos, NM 87505, USA.

## Materials and Methods

**Crystallization, data collection, and processing.** All purified recombinant *Pseudomonas fluorescens* ICH proteins were expressed from pET15b constructs and contain the vector-derived amino acids “GSH” at the N-terminus as a result of thrombin cleavage of the N-terminal 6xHis tag, as previously described (1). The G150A and G150T mutants were made by site-directed mutagenesis using mutagenic primers and were verified by DNA sequencing. Wild-type, G150A, and G150T ICH were crystallized by hanging drop vapor equilibration by mixing 2  $\mu$ L of protein at 20 mg/ml and 2  $\mu$ L of reservoir (23% PEG 3350, 100 mM Tris-HCl, pH 8.6, 200 mM magnesium chloride and 2 mM dithiotheritol (DTT)) and incubating at 22°C. Spontaneous crystals in space group P2<sub>1</sub> appear in 24-48 hours and were used to microseed other drops after 24 hours of equilibration. Microseeding was used because two different crystal forms of ICH crystals sometimes grow in the same drop and those in space group P2<sub>1</sub> are the better-diffracting crystal form. Notably, seeding G150T ICH using wild-type ICH crystals in space group P2<sub>1</sub> results exclusively in G150T crystals in space group C2 with one molecule in the asymmetric unit (ASU).

Cryogenic (100K) synchrotron data (PDB 3NON) were collected at the Advanced Photon Source beamline 14BM-C from plate-shaped crystals measuring ~500x500x150  $\mu$ m that were cryoprotected in 30% ethylene glycol, mounted in nylon loops, and cooled by immersion in liquid nitrogen as previously described (1). Ambient temperature (274 K and 277 K) synchrotron data sets were collected at the Stanford Synchrotron Radiation Lightsource from crystals mounted in 0.7 mm diameter, 10  $\mu$ m wall thickness glass number 50 capillaries (Hampton Research) with a small volume (~5  $\mu$ L) of the reservoir to maintain vapor equilibrium. Excess liquid was removed from the crystal by wicking, and the capillary was sealed with beeswax. For the 274 K dataset, the crystal was mounted with its shortest dimension roughly parallel to the capillary axis, resulting in the X-ray beam shooting through the longest dimensions of the crystal during rotation. For the 277 K dataset, a large single capillary-mounted crystal was exposed to X-rays and then translated so that multiple fresh volumes of the crystal were irradiated during data collection. This strategy reduces radiation damage by distributing the dose over a larger volume of the crystal. This translation of the sample was factored into the absorbed dose calculation by assuming every fresh volume of the crystal received no prior dose, which is a best-case scenario.

The 100 K and 277 K datasets were collected on ADSC Q4 CCD detectors using the oscillation method. Separate low and high resolution passes were collected with different exposure times and detector distances and merged together in scaling, as the dynamic range of the diffraction data was larger than that of the detector. For the 274 K data, a Pilatus 6M pixel array detector (PAD) was used with shutterless data collection. Because of the very high dynamic range of the detector, a full dataset was collected in a single pass of ~5 minutes. The 274 K datasets were indexed and scaled using XDS (2) while the 277K datasets were indexed and scaled using HKL2000 (3). The 100 K dataset was processed as previously described (1).

**Microcrystal growth and XFEL sample delivery.** For the XFEL experiment, microcrystals of ICH were grown by seeding. Initial seeds were obtained by pulverizing macroscopic crystals via vortexing with several 0.5 mm stainless steel balls for 5 minutes. A dilution of this seed stock was added to 31% PEG 3350, 250 mM MgCl<sub>2</sub>, 125 mM Tris-HCl pH=8.8, then an equal volume of 40 mg/ml ICH in 25 mM HEPES pH 7.5, 100 mM KCl was added and rapidly mixed. The dilution of the seed stock dictated the final size of the microcrystals and was optimized to produce crystals measuring ~20  $\mu$ m x 20  $\mu$ m x 2  $\mu$ m. The mixture was incubated at room temperature with gentle shaking for ~20 minutes until microcrystal growth stopped.

Samples were delivered to the beam using the concentric-flow microfluidic electrokinetic sample holder (coMESH) injector (4) under atmospheric pressure conditions at room temperature and under normal atmosphere. The sample was loaded in a custom stainless steel sample reservoir. A Shimadzu LD20 HPLC pump hydraulically actuated a teflon plunger to advance the sample slurry. A stainless steel 20  $\mu\text{m}$  frit filter (IDEX-HS) was placed after the reservoir in order to ensure smaller crystal sizes and mitigate clogging. The reservoir and filters were connected to the coMESH via a 100  $\mu\text{m}$  x 160  $\mu\text{m}$  x 1.5 m fused silica capillary (Molex). This capillary continued unobstructed through the center of the microfluidic tee (Labsmith) and terminated at 0 mm, 2 mm, or 200 mm recessed from the exit of a concentric 250  $\mu\text{m}$  x 360  $\mu\text{m}$  capillary, corresponding to substrate-free (Free), 15 s and 5 min time delays, respectively. The capillaries were optically aligned to obtain a 0 offset, then were recessed and measured externally to achieve the 2 mm and 200 mm recess. In the case of the longer 200 mm offset, an additional tee (IDEX-HS) was added to increase the length.

The outer line of the coMESH flowed the stabilizing solution (31% PEG 3350, 250 mM MgCl<sub>2</sub>, 125 mM Tris-HCl pH=8.8) in the case of the Free structure, and flowed ~2 mM p-NPIC substrate in stabilizing solution for the 15 s and 5 min timepoints. DTT was omitted from all solutions as p-NPIC is not stable its presence and the p-NPIC substrate was at saturation (estimated concentration is ~2 mM) in this solution. The p-NPIC substrate was loaded into a 500 or 1000  $\mu\text{L}$  gas tight syringe (Hamilton). The stainless steel, blunt tip removable needle was connected to a 250  $\mu\text{m}$  x 360  $\mu\text{m}$  x 1 m fused silica capillary (Molex) and connected to the side of the coMESH microfluidic tee junction for the Free and 15 s delay and into the side of the Idex tee for the 5 minute delay. The syringe was driven by a syringe pump (KDS Legato 200) at 1-2  $\mu\text{l}/\text{min}$  while being charged at 3.1 kV (Stanford Research Systems, SRS PS300) at the wetted stainless steel needle.

The outer liquid focused the fluids ~500  $\mu\text{m}$  away from the outer capillary towards the XFEL focus of approximately 3  $\mu\text{m}$  at the Macromolecular Femtosecond Crystallography (MFX) endstation. The charged meniscus was approximately 5 mm away from a grounded counter electrode to complete the electrokinetic focusing. The time delays were assumed to be sufficiently long as compared to the electrokinetic mixing phenomena and were determined simply by the time the bulk fluid would traverse the offset distance. The flow rates and voltages were held constant during each time point and the flow of the crystals were optically monitored with a 50x objective to assure minimal flow deviations. For the Free (no delay) time point, the flow was 0.5  $\mu\text{l}/\text{min}$  for both the sample and outer flows. For the 15 s time delay, the capillaries were recessed 2 mm, and the flows were 1 and 2  $\mu\text{l}/\text{min}$  for the sample and p-NPIC flow rates, respectively. The combined bulk flows (1+2 = 3  $\mu\text{l}/\text{min}$ ) and the 2 mm offset dictated the delay time of 15 s. For the 5 min time delay, the capillaries were offset 200 mm and both flow rates were held at 1  $\mu\text{L}/\text{min}$ , for a combined bulk flow of 2  $\mu\text{L}/\text{min}$ . Overall, ~0.5 mL of sample crystals and 0.5 mL of 2 mM p-NPIC were consumed to gather this data.

### XFEL data collection, and processing

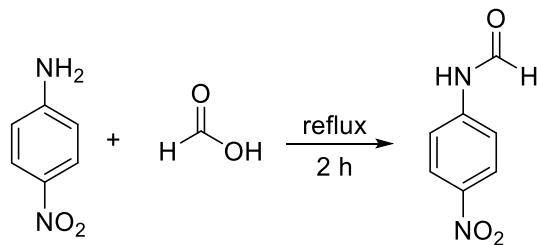
Data were collected at the MFX endstation of the Linac Coherent Light Source (LCLS). X-ray pulses were 9.5 keV,  $\sim 1 \times 10^{12}$  photons per 40 fs pulse at 30 Hz repetition. Beam size at sample was ~3  $\mu\text{m}$ . Diffraction data were collected on a Rayonix MX340-XFEL CCD detector operated in 4x4 binning mode and hits were analyzed in real time using OnDA (5). The XFEL diffraction data were processed with cctbx.xfel (6), to identify 76,174 crystal hits for the Free data, 53,476 crystal hits for the 15 s delay data and 36,875 crystal hits for the 5 min delay data. A small fraction of multiple lattice hits (<0.01% of total) were shown to have little impact on data quality when included in the final post-refinement steps. For the Free data, 23,669 frames were indexed and 21,834 of those had their intensities merged and integrated. For the 15 s data,

26,507 frames were indexed and 24,286 of those had their intensities merged and integrated. For the 5 min data, 16,893 frames were indexed and 14,483 of those had their intensities merged and integrated. To correct the intensity measurements and merge the data, postrefinement was carried out with three cycles of PRIME (7) using model unit cell dimensions from a synchrotron wild type ICH structure (1). The Lorentzian partiality model used parameters  $\text{gamma\_e} = 0.001$ ,  $\text{frame\_accept\_min\_cc} = 0.60$ ,  $\text{uc\_tolerance} = 5$ ,  $\text{sigma\_min} = 2.5$ , and  $\text{partiality\_min} = 0.2$ . The X-ray crystallographic data statistics for all datasets are provided in SI Appendix Table S2.

**Selection of mix-and-inject X-ray time delays.** We collected absorbance spectra of ICH crystals in reservoir solution supplemented with 1 mM p-NPIC and 40% glycerol using UV-vis microspectrophotometry at SSRL BL 11-1 (SI Appendix Figure S1). We freeze-trapped the reaction in the cryostream at fixed time-delays after adding substrate to the crystal before collecting a spectrum. The p-NPIC absorption maximum is ~270 nm, while p-nitrophenyl formamide product absorption maximum is ~315 nm on this instrument. The lack of an isosbestic point suggests an intermediate is present. At a time delay of 15 s, the substrate peak at 270 nm had disappeared, while the product peak at 315 nm had not formed yet. At 5 min, substrate is exhausted while the product peak at 315 nm had fully formed, informing the timing for the XFEL experiment. The macroscopic ( $\sim 2 \times 10^6 \mu\text{m}^3$ ) crystals from which these spectra were collected were damaged by exposure to substrate and did not diffract X-rays well after substrate was introduced, precluding a cryotrapping X-ray diffraction experiment. In contrast, the microcrystals used for the XFEL experiment ( $\sim 1 \times 10^3 \mu\text{m}^3$ ) were not damaged by substrate, necessitating a serial X-ray crystallography approach.

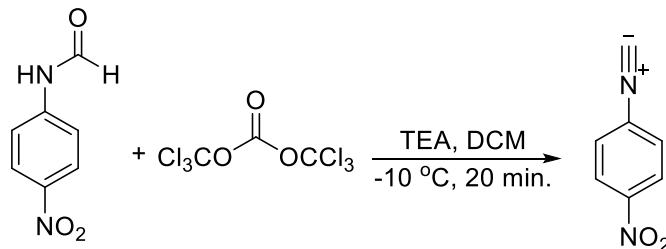
**Crystallographic model refinement.** All refinements were performed in PHENIX against structure factor intensities including individual atomic displacement parameters (ADPs) and riding hydrogen atoms in the model (8). Weights for the ADP refinement and relative weights for the X-ray and geometry term were optimized. For the ambient temperature synchrotron data at  $\sim 1.1 \text{ \AA}$  resolution, anisotropic ADPs were refined. For the  $1.55 \text{ \AA}$  resolution XFEL datasets, translation-libration-screw (TLS) refinements (9) with automatic rigid body partitioning were performed, followed by residual isotropic ADP refinement. For the Cys101-SOH and G150A ICH synchrotron datasets, the alternate conformation for helix H (residues 148-173 in chain A) was modeled as a single occupancy group, reflecting the presumed correlated displacement of sidechain and backbone atoms. Other disordered regions were also built into multiple conformations manually in COOT (10) if supported by  $2mF_o - DF_c$  and  $mF_o - DF_c$  electron density maps. Occupancies of these groups were refined but constrained to sum to unity in PHENIX. Omit maps were calculated after removing the areas of interest from the model and refining for three macrocycles. Final models were validated using MolProbity (11) and the validation tools in COOT and PHENIX. Model statistics are provided in SI Appendix Table S3. Isomorphous difference maps ( $F_o(15\text{s}) - F_o(\text{XFEL}_{\text{FREE}})$  and  $F_o(\text{SR}) - F_o(\text{XFEL}_{\text{FREE}})$ ) were calculated using data to the lowest common resolution cutoff of the data sets,  $1.55 \text{ \AA}$ . Structure factor data and refined coordinates are available in the Protein Data Bank with the following accession codes: 6NI4, 6NI5, 6NI6, 6NI7, 6NI8, 6NI9, 6NJA, 6NPQ, 6UND, and 6UNF.

**Synthesis of para-nitrophenyl isocyanide (p-NPIC).** ICH will accept diverse isocyanide substrates (12). Due to its convenient UV-visible spectral properties ( $\lambda_{\text{max}}=320 \text{ nm}$ ), para-nitrophenyl isocyanide (p-NPIC) was used here. The p-NPIC substrate is not commercially available and was synthesized by dehydration of the N-formamide precursor. To synthesize N-(4-Nitrophenyl)formamide, a mixture of amine (10 mmol) and formic acid (12 mmol) was stirred at  $60^\circ\text{C}$  for 2h.



After completion of the reaction as judged by thin layer chromatography (TLC), the mixture was diluted with  $\text{CH}_2\text{Cl}_2$  (100 mL), washed with saturated solution of  $\text{NaHCO}_3$  and brine (100 mL), dried over anhydrous  $\text{Na}_2\text{SO}_4$ , and concentrated under reduced pressure. The residue was dissolved in hot acetone and crystallized to yield N-(4-Nitrophenyl)formamide (1.58 g, 96%) as a yellow solid. The product was verified using  $^1\text{H}$  NMR,  $^{13}\text{C}$  NMR, IR, and Time of Flight (TOF) mass spectra.

To synthesize p-nitrophenyl isocyanide, the aforementioned N-(4-Nitrophenyl)formamide product (8.0 mmol) and triethylamine (56 mmol) were dissolved in  $\text{CH}_2\text{Cl}_2$  (30 mL) and cooled to -10 °C.



A solution of triphosgene (8.0 mmol) in  $\text{CH}_2\text{Cl}_2$  (50 mL) was slowly added and stirring was continued at -10 °C for another 30 minutes. After completion of reaction (judged by TLC), the reaction mixture was passed through a pad of silica gel and washed with  $\text{CH}_2\text{Cl}_2$ . The filtrate was dried over anhydrous  $\text{Na}_2\text{SO}_4$  and concentrated under reduced pressure. The residue was triturated with cold hexane to yield para-nitrophenyl isocyanide (1.36 g, 92%) as a yellow solid.  $^1\text{H}$  NMR,  $^{13}\text{C}$  NMR, IR, and Time of Flight (TOF) mass spectra were collected to verify the product structure. The para-nitrophenyl isocyanide product was stored as a dry solid at -80°C until needed.

**ICH enzyme kinetics.** Steady state ICH rate measurements were initiated by the addition of ICH (final concentration of 1  $\mu\text{M}$ ) to freshly prepared p-NPIC solutions ranging from 0-60  $\mu\text{M}$  in reaction buffer (100 mM  $\text{KPO}_4$  pH=7.0, 50 mM KCl, and 20% DMSO). p-NPIC was diluted from a freshly prepared 0.5 M stock solution in dimethyl sulfoxide (DMSO), which was stored at -80 °C and protected from light when not in use. A 200  $\mu\text{l}$  reaction was maintained at 25 °C in a Peltier-thermostatted cuvette holder. The formation of the product, para-nitrophenyl formamide (p-NPF) was monitored at its absorption maximum of 320 nm for two minutes using a UV-Vis Cary 50 Spectrophotometer (Varian, Palo Alto, CA). A linear increase in  $A_{320}$  was verified and used to calculate initial velocities. Isocyanides can spontaneously hydrolyze slowly in aqueous solutions, with the rate increasing as pH is lowered. To ensure that all measured product formation was due to ICH catalysis, the rate of spontaneous p-NPIC hydrolysis was measured in the absence of ICH. These values were near the noise level of the spectrophotometer and were subtracted from the raw rate measurements before fitting the Michaelis-Menten model. The extinction coefficient at 320 nm for p-NPF was determined by using ICH to convert known concentrations of p-NPIC to p-NPF, followed by measuring the absorbance at 320 nm. The slope of the resulting standard curve was defined as the extinction coefficient of p-NPF at 320 nm;  $\epsilon_{320}=1.33\times 10^4 \text{ M}^{-1} \text{ cm}^{-1}$ . This p-NPF  $\epsilon_{320}$  value was used to

convert the measured initial velocities from  $A_{320}/\text{sec}$  to  $[p\text{-NPF}]/\text{sec}$ . All data were measured in triplicate or greater and mean values and standard deviations were plotted and fitted using the Michaelis-Menten model as implemented in Prism (GraphPad Software, San Diego, CA). Reported  $K_m$  and  $k_{\text{cat}}$  values and their associated errors are given in SI Appendix Figure S8.

Pre-steady state ICH kinetics were measured at 25 °C using a Hi-Tech KinetAsyst stopped flow device (TgK Scientific, Bradford-on-Avon, United Kingdom). Data were collected for each sample for two seconds (instrument deadtime is 20 ms) in triplicate. The final enzyme concentration after mixing was 10 μM and final p-NPIC concentrations were 20, 40, 80, 120, 160, and 320 μM. Product evolution was monitored at 320 nm using a photodiode array detector. Kinetic Studio software (TgK Scientific, United Kingdom) was used to analyze the kinetic data and to fit a mixed model containing a single exponential burst with a linear steady state component:  $-A\exp(-kt) + mt + C$ . In this equation,  $t$  is time,  $k$  is the burst phase rate constant,  $m$  is the linear phase (steady-state) rate,  $A$  is the amplitude of the burst component, and  $C$  is a baseline offset constant. The linear slope  $m$  was used to calculate steady state turnover numbers, which agree well with  $k_{\text{obs}}$  values obtained from steady state kinetic measurements at comparable substrate concentrations. Single turnover experiments were also performed using final concentrations of 40 μM enzyme and 20 μM p-NPIC after manual mixing. Spectra were collected using a Cary 50 spectrophotometer (Varian, Palo Alto, CA, USA). Spectra were collected every 10 seconds with a deadtime of ~30 seconds after manual addition of enzyme.

**Molecular Dynamics Simulations.** An ICH dimer model was protonated at pH 7.0 and minimized under the OPLS3 force field using the Schrödinger 2018-3 software suite [Schrödinger Suite 2018-3 Protein Preparation Wizard; Schrödinger, LLC, New York, NY, 2016]. ICH crystals were parameterized using Amber (13). A simulation cell with unit cell dimensions and  $P2_1$  symmetry of the crystal structure was created and replicated to obtain a 2x2x2 supercell containing 16 ICH dimers to minimize boundary artifacts in the simulations. 200 mM MgCl<sub>2</sub> and 100mM Tris-HCl were added to the simulation cell. While the crystallization conditions also included PEG3350 and DTT, those were omitted from the simulation owing to the large size of PEG and the low concentration (2 mM) of DTT. The system was electrostatically neutralized by adding Na<sup>+</sup> ions. SPC/E waters were added to obtain a pressure of approximately 1 bar. Simulations of 'XFEL conditions' were started from the XFEL crystal structure, with C101 in the thiolate (Cys101-S<sup>−</sup>) state. By contrast, the synchrotron structure was simulated by modifying C101 to Cys-sulfenic acid (Cys101-SOH) in the XFEL structure and removing the crystallographic ordered water molecule near Asp17. Partial charges for Cys-SOH were determined with HF/6-31G\* basis set and the AM1-BCC method in Antechamber (14). The systems were minimized with steepest descent and conjugate gradient algorithms by gradually reducing constraints on the protein atoms, and heated (NVT) to 300 K over 10 ps. The time step was set to 1 fs for heating and the initial phase of equilibration. Production runs of 1 μs ICH crystal NVT ensembles were carried out at 300 K with openMM (15) on NVIDIA K80 and P100 GPUs, with a Langevin thermostat (friction coefficient 1.0), an integration timestep of 2 fs, and non-bonded cutoffs of 1 nm. In total, we obtained 4 μs of simulation time for ICH.

The distance of the I152<sub>H</sub>-C101<sub>SG</sub> hydrogen bond was calculated for each protomer at time intervals of 500 ps over the course of the simulations. The average I152<sub>H</sub>-C101<sub>SG</sub> distance was obtained by averaging over the protomers (bold line, Figure 3b), and then averaging over time. The shifts of helix H were calculated at time intervals of 500 ps by first aligning each protomer to the first frame using all backbone (heavy) atoms giving an RMSD<sub>REF</sub>, and then calculating the backbone (heavy) atom RMSD to the first frame over residues 152 to 166 giving

$\text{RMSD}_{\text{HELIX}}$ . We then reported the fraction  $\text{RMSD}_{\text{HELIX}} / \text{RMSD}_{\text{REF}}$ . While RSMD strongly depends on the length of the fragment and flexible loops, generally  $\text{RMSD}_{\text{HELIX}} / \text{RMSD}_{\text{REF}} > 1$  indicates that the helix shifts more than the rest of the protomer. The average shift was obtained by averaging over the protomers (bold line, Figure 3c), and then averaging over time.

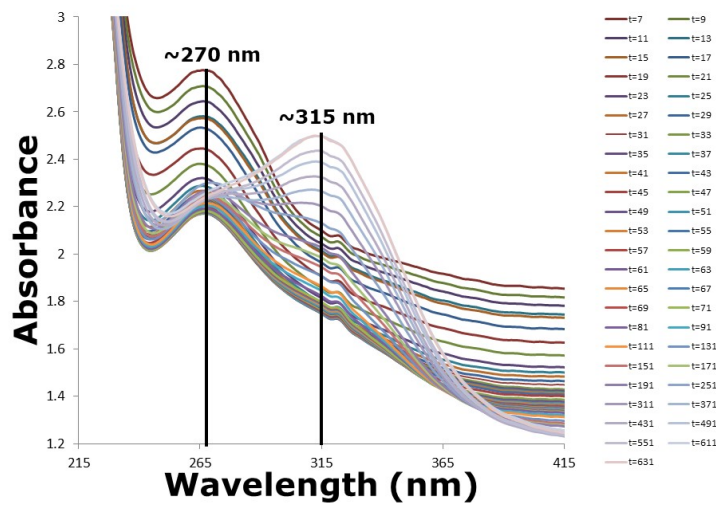


**Figure S1. *In crystallo* UV-visible spectrophotometry of ICH catalysis.** A single crystal of ICH was mixed with 1 mM p-NPIC, incubated for the indicated times in seconds, mounted and cryocooled to 100 K in a nitrogen cryostream. Absorbance spectra were collected using the inline spectrophotometer at BL 11-1 at the Stanford Synchrotron Radiation Lightsource (SSRL). On this instrument, the p-NPIC substrate has an absorption maximum of 270 nm and the p-NPF product has an absorption maximum of 315 nm. Note the absence of an isosbestic point.

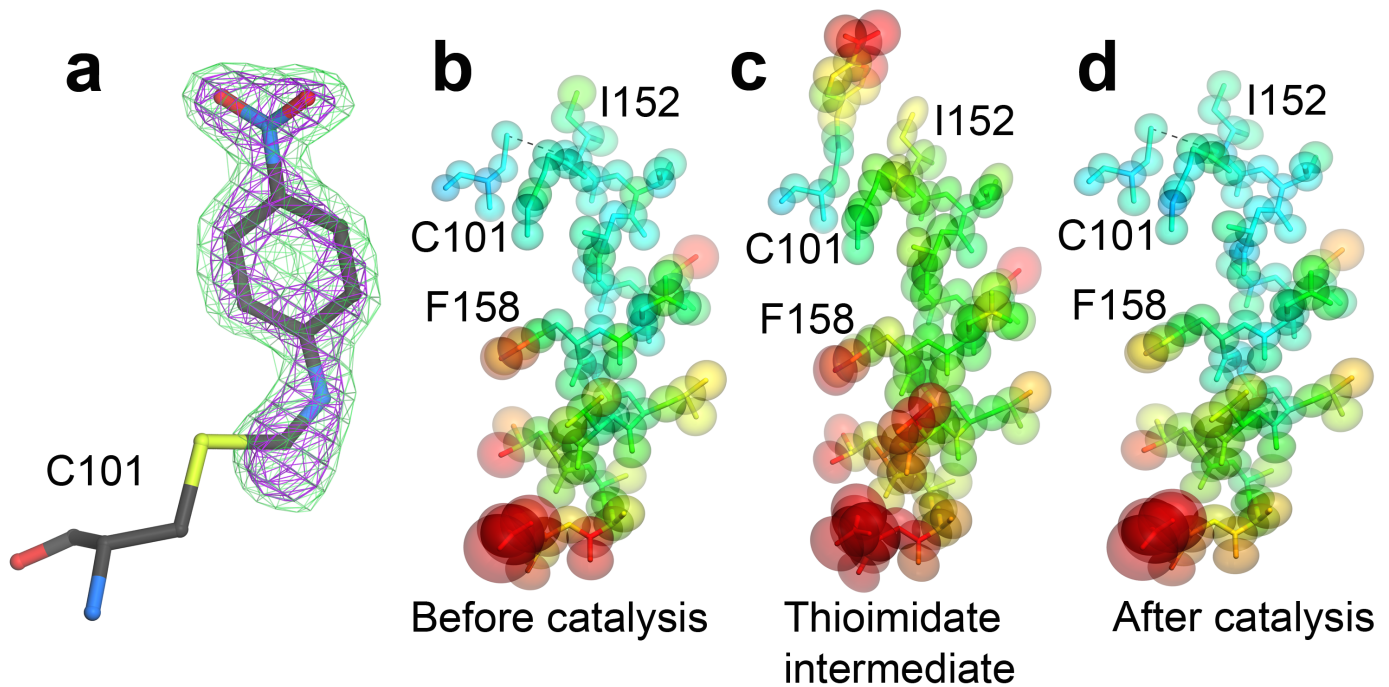


**Figure S2. Observation of thioimide intermediate formation and enhancement of ICH helix mobility.** In (a), omit  $mF_o-DF_c$  electron density is shown at 3.0 rmsd (green) and 5.0 rmsd (purple), unambiguously demonstrating presence of the catalytic intermediate. In (b-d), anisotropic atomic displacement parameters (ADPs) from TLS models refined against the XFEL datasets are shown at the 75% probability level and colored according to  $B_{eq}$  value, from blue ( $7 \text{ \AA}^2$ ) to red ( $30 \text{ \AA}^2$ ). Starting with the resting enzyme before substrate is introduced (b), helical mobility is transiently elevated upon thioimide intermediate formation during catalysis (c) and then is reduced again upon completion of catalysis (d) once substrate is consumed 5 minutes after mixing.

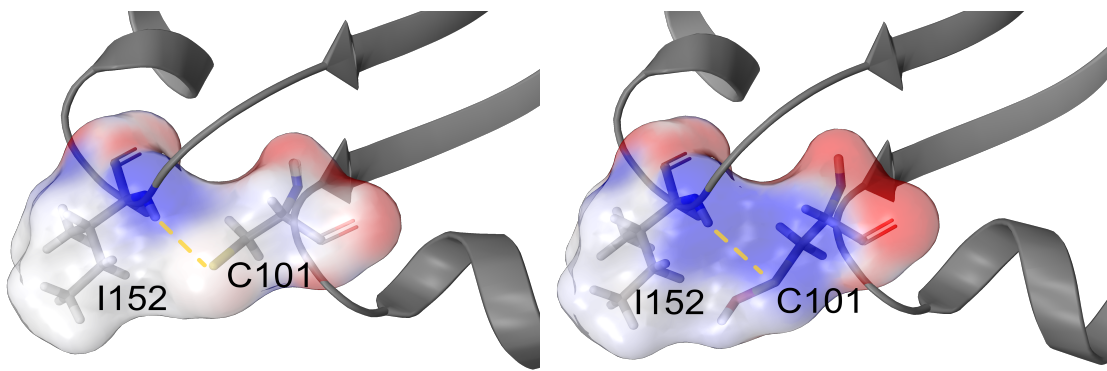


**Figure S3. Cys101 oxidation leads to a weakening of the Ile152-Cys101 H-bond.** Electrostatic Poisson-Boltzmann surfaces (red negative, blue positive charge) calculated for Cys101-S-Ile152 (left) and Cys-SOH-Ile152 (right). Cysteine photooxidation neutralizes the negative charge of the thiolate sulfur atom, weakening the N-H ... S hydrogen bond. We calculated a reduction in the Cys101-Ile152 hydrogen bond energy from -2.2 kcal/mol under reduced conditions (i.e. with a thiolate acceptor) to -0.91 kcal/mol upon Cys101-SOH formation.

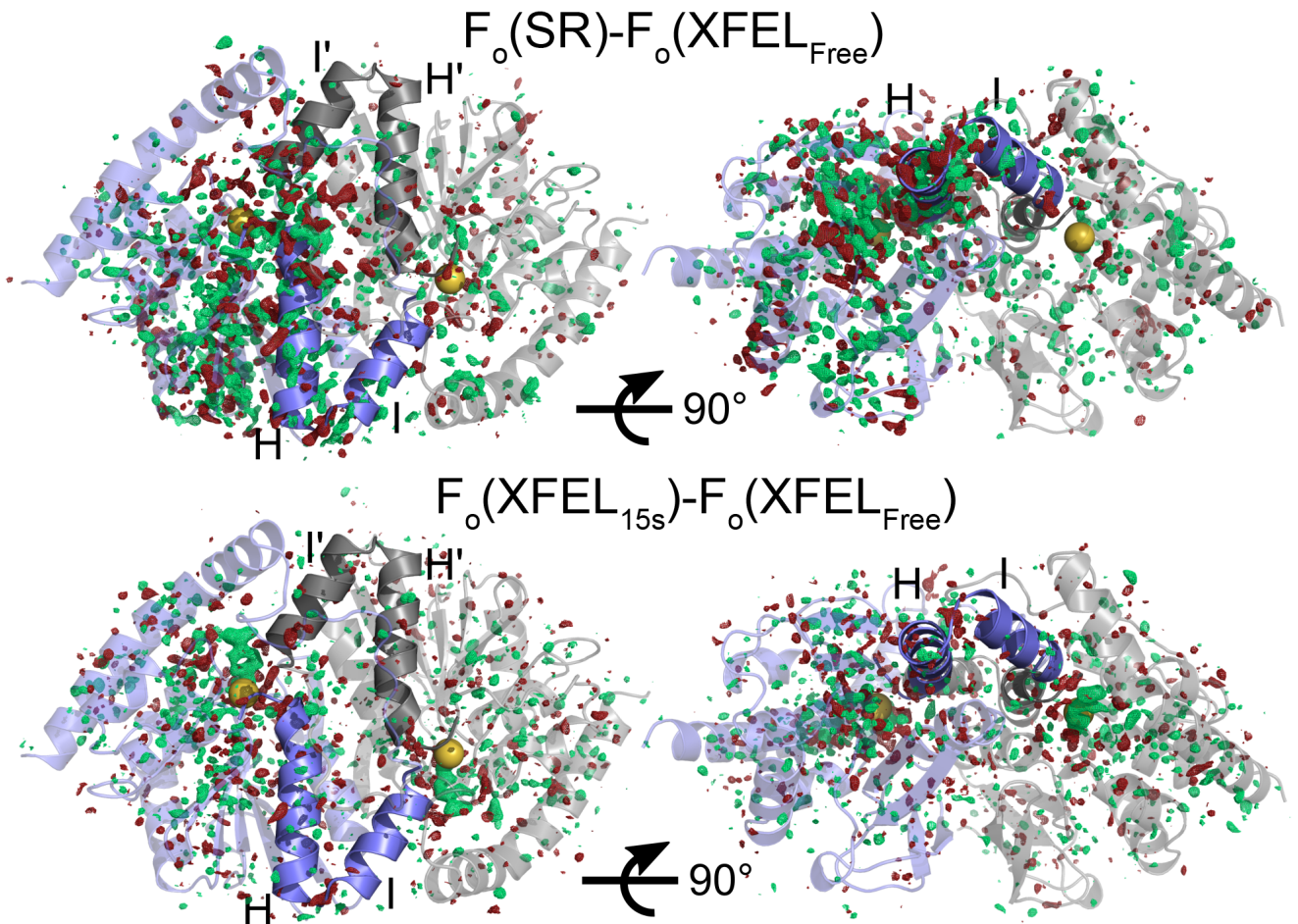


**Figure S4. Isomorphous difference maps show widely distributed conformational changes upon cysteine modification.**  $F_o(\text{SR}) - F_o(\text{XFEL}_{\text{Free}})$  (top panels) and  $F_o(\text{XFEL}_{15\text{s}}) - F_o(\text{XFEL}_{\text{Free}})$  (bottom panels) difference maps are contoured at 2.75 rmsd. Difference features (green, positive; red, negative) are non-uniformly distributed in both maps, radiating out from the site of the catalytic nucleophile (yellow spheres). This is more pronounced in the A protomer (slate blue) than the B protomer (grey) in the  $F_o(\text{SR}) - F_o(\text{XFEL}_{\text{Free}})$  map (top panels). Difference features generally show the same, but weaker pattern in the  $F_o(\text{XFEL}_{15\text{s}}) - F_o(\text{XFEL}_{\text{Free}})$  map, where the 15 s timepoint corresponds to thioimidate intermediate formation. The maps are phased with the Free (no substrate) XFEL structure.

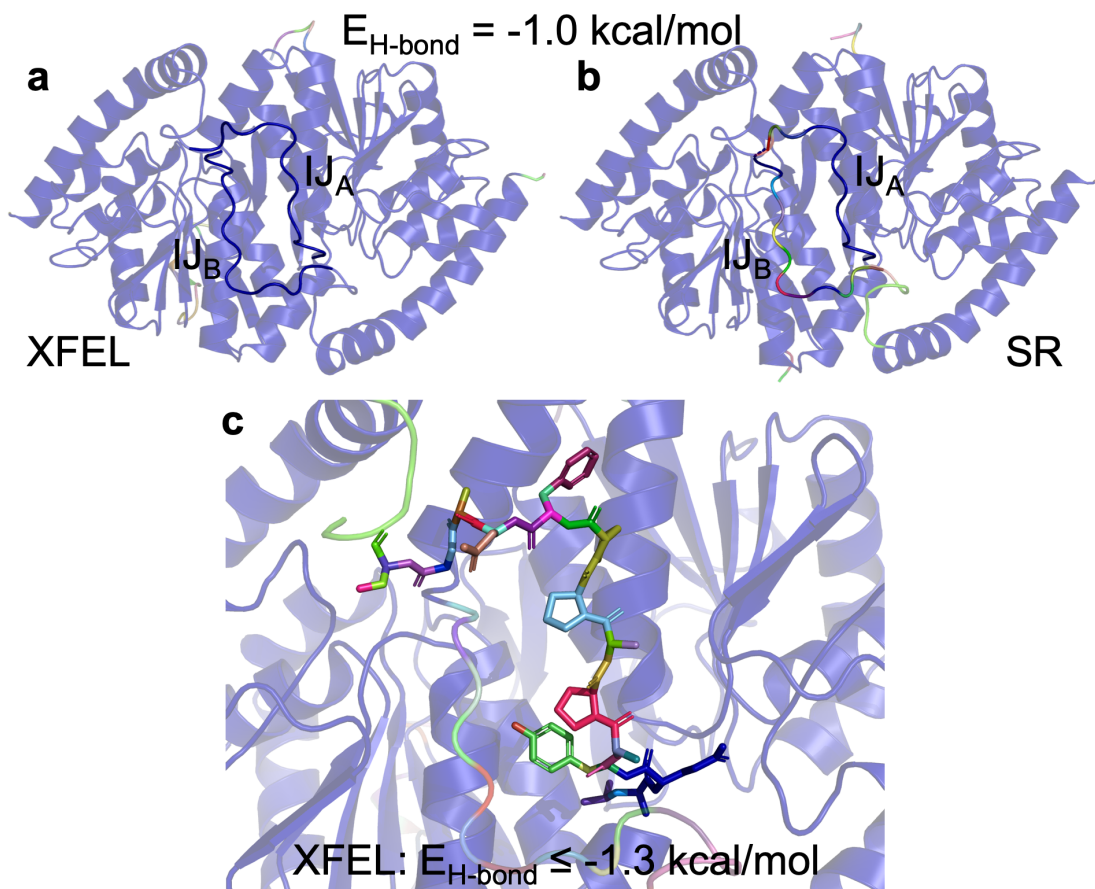


**Figure S5. Rigidity Analysis.** Individual rigid clusters are color-coded. In both the XFEL (a) and SR (b) structures, the backbone is largely rigidified (blue color). (a) ICH XFEL structure. The IJ<sub>A</sub> and IJ<sub>B</sub> linkers are rigid in the XFEL structure when H-bonds stronger than -1 kcal/mol are included in the analysis, with the C101:S-I152:NH bond constraint in both protomers. (b) ICH SR structure. The IJ<sub>B</sub> linker, which contacts helix H, becomes flexible in the SR structure with the shifted conformation of helix H. (c) When H-bonds weaker than -1.3 kcal/mol are excluded, both linkers IJ<sub>A</sub> and IJ<sub>B</sub> become flexible. Interestingly, these are the first structural elements of ICH to melt when weaker H-bonds are omitted.

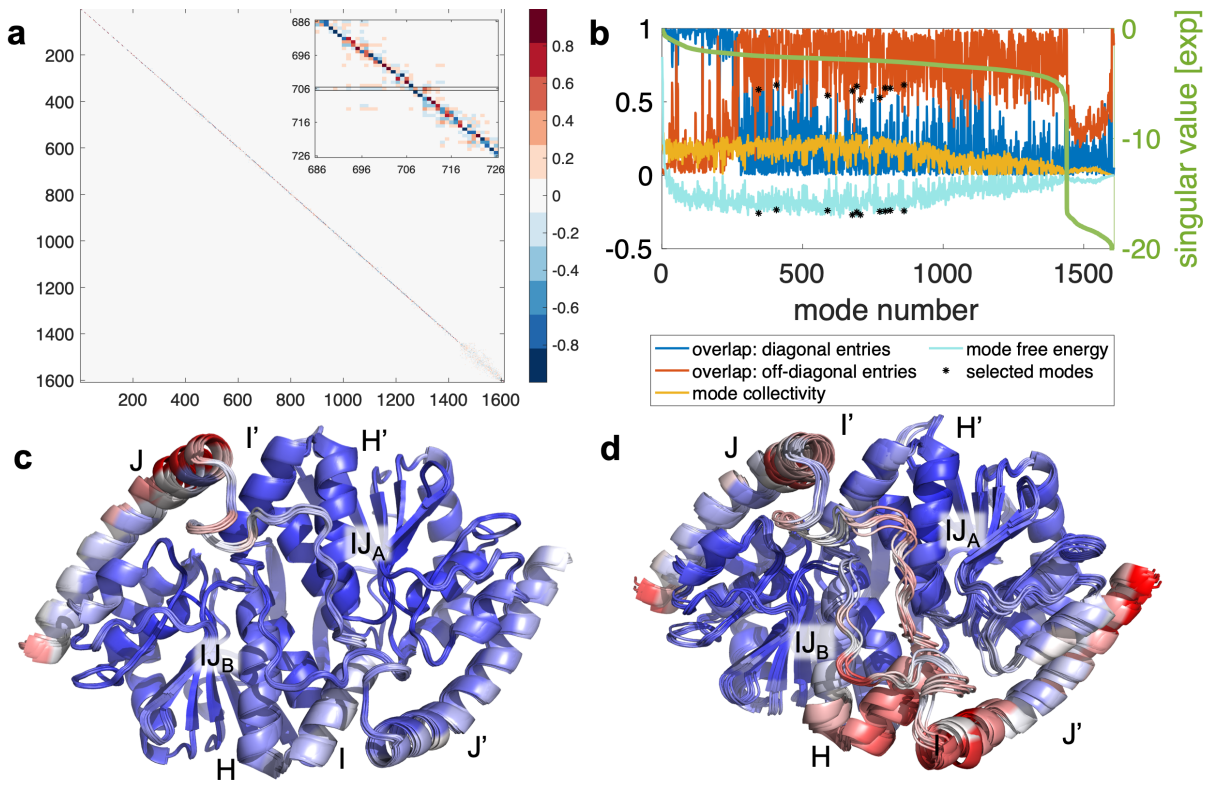


**Figure S6. Kinematic flexibility analysis of ICH.** (a) Visualization of the matrix product  $D = V_B^T V_{A\&B}$ . The matrix  $D$  reports on the mode overlap when the Cys101 hydrogen bond is present only in the B protomer (vertical) vs. in both protomers (horizontal) of the XFEL structure. Motion vector dot products are color coded between -1 and 1 (color bar). The inset highlights an area around one of the modes with lowest mode-specific free energy and least overlap to any other mode (mode 706, insert). (b) Motion modes that are least similar between the XFEL and SR structures. The mode-specific free energy (teal) is the difference between internal energy perturbation (singular values in green line) and conformational entropy (mode collectivity, yellow) computed as the normalized exponential of the Shannon entropy. From a set of 100 modes with lowest free energy (teal), we select the top ten modes with least overlap (red and blue) to any other mode. For each of these modes, the two stars indicate their mode-specific free energy and their maximum diagonal (blue) or off-diagonal (red) overlap to any other mode. (c-d) Variations in ICH motional spectrum and inter-protomeric exchange upon Cys101 H-bond modification. (c) Conformational ensemble of motion modes in Kinematic Flexibility Analysis enriched after the C101<sub>SG</sub>-I152<sub>H</sub> H-bond in the A protomer is disrupted. Consistent with the MD simulations, the IJ linkers in both conformers, which are in contact with helices H, show increased conformational dynamics, especially near both active sites. Motion modes associated with helix H and, in particular, I, and helices J and J' are also enriched. (d) For comparison, we also selected ten randomly selected KFA orthogonal motion modes with mode numbers < 300 or > 1,000 (elevated mode-specific free energies) and computed their associated motions with the same step size. These motions are less focused, and engage the entire protein. The conformational ensembles are projected onto the XFEL structure and colored by RMSF, increasing from blue to red.

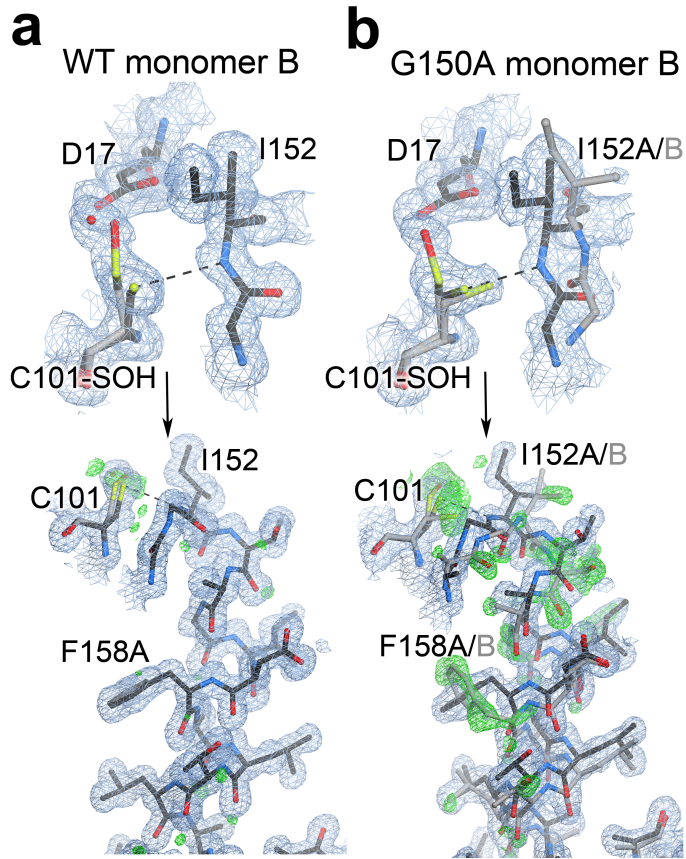


**Figure S7: Helical mobility is asymmetric in wild-type but not G150A ICH.** The top panels show the environment of Cys101 in the second protomer (“protomer B”) of wild-type (WT) and G150A ICH. 2mF<sub>o</sub>-DF<sub>c</sub> electron density is contoured at 0.7 RMSD (blue) and the hydrogen bond between the peptide backbone of Ile152 and Cys101 is shown in a dotted line. The lower panels show the helix in its strained (black) and relaxed, shifted conformations (grey). 2mF<sub>o</sub>-DF<sub>c</sub> electron density is contoured at 0.8 RMSD (blue) and omit mF<sub>o</sub>-DF<sub>c</sub> electron density for the shifted helical conformation is contoured at 3.0 RMSD (green). Wild-type ICH does not show strong evidence of a second conformation, even though Cys101 has been partially photooxidized to Cys101-SOH (top). In contrast, the helix in monomer B of G150A ICH shows strong evidence of a second, relaxed conformation, similar to monomer A.

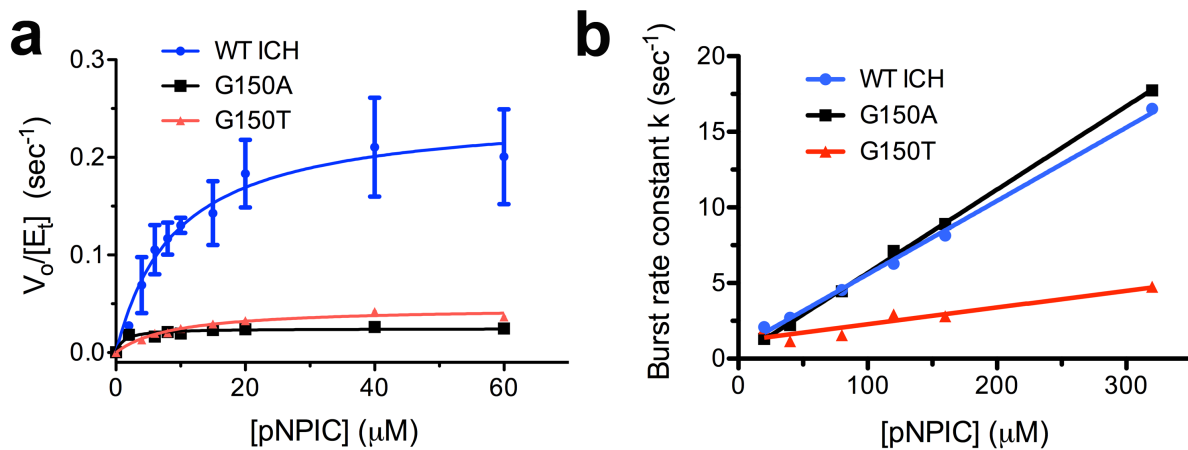


**Figure S8: G150 mutations impair ICH catalysis.** Steady-state (a) and pre-steady state (b) enzyme kinetics of wild-type (WT; blue circles), G150A (black squares), and G150T (red triangles) ICH. Both the G150A and G150T mutations result in similar decreases in steady-state kinetics compared to WT enzyme ( $k_{\text{cat}}(\text{WT})=0.248\pm0.031 \text{ s}^{-1}$ ,  $k_{\text{cat}}/K_M(\text{WT})= 2.68\times10^4 \text{ M}^{-1}\text{s}^{-1}$ ;  $k_{\text{cat}}(\text{G150A})=0.025\pm0.002 \text{ s}^{-1}$ ,  $k_{\text{cat}}/K_M(\text{G150A})=2.07\times10^4 \text{ M}^{-1}\text{s}^{-1}$ ;  $k_{\text{cat}}(\text{G150T})=0.046\pm0.003 \text{ s}^{-1}$ ,  $k_{\text{cat}}/K_M(\text{G150T})= 5.21\times10^3 \text{ M}^{-1}\text{s}^{-1}$ ). (b) The burst rate constant in pre-steady state kinetics is linearly dependent on substrate concentration. This linear dependence indicates a second order rate process during the burst phase, consistent with thioimide intermediate formation. WT and G150A have similar second order burst rate constants ( $k(\text{WT})=4.85\times10^4\pm943 \text{ M}^{-1}\text{s}^{-1}$ ;  $k(\text{G150A})= 5.51\times10^4\pm557 \text{ M}^{-1}\text{s}^{-1}$ ), but G150T ICH is lower ( $k(\text{G150T})= 1.11\times10^4\pm999 \text{ M}^{-1}\text{s}^{-1}$ ).

**Video S1: Molecular dynamics simulation trajectory for ICH.** Motion of helix H in a molecular dynamics trajectory of the Cys101-SOH ICH dimer is shown. Shadowing of the initial conformation is included to highlight the downward shift of helix H in protomer A (left).

**Table S1: Enzyme kinetic parameters**

Enzyme	WT	G150A	G150T
<b>Steady State Kinetics</b>			
$k_{cat}$ (sec <sup>-1</sup> )	0.248±0.031	0.025±0.002	0.046±0.003
K <sub>M</sub> (μM)	9.262±3.250	1.208 ±0.6134	8.892±1.529
$k_{cat}/K_M$ (M <sup>-1</sup> sec <sup>-1</sup> )	2.68x10 <sup>4</sup>	2.07x10 <sup>4</sup>	5.21x10 <sup>3</sup>
<b>Stopped Flow mixing</b>			
Burst rate constant (sec <sup>-1</sup> ) <sup>*</sup>	11.395±0.120	11.882±0.071	4.255±0.187
Second order rate constant for burst (M <sup>-1</sup> sec <sup>-1</sup> )	4.85x10 <sup>4</sup> ±943	5.51x10 <sup>4</sup> ±557	1.11x10 <sup>4</sup> ±999
Steady state rate k <sub>obs</sub> (sec <sup>-1</sup> ) <sup>*</sup>	0.268±0.001	0.046±0.002	0.095±0.003

\*measured at 160 μM p-NPIC

Standard deviations are derived from the fit; data measured n≥3

**Table S2: Crystallographic Data Statistics**

Sample	WT ICH RT <sup>1</sup> (less oxidized)	WT ICH RT <sup>1</sup> (more oxidized)	G150A ICH	G150T ICH	WT ICH XFEL: Free <sup>1</sup>	WT ICH XFEL: 15 sec Thioimidat e <sup>1</sup>	WT ICH XFEL: 5 min <sup>1</sup>	WT ICH cryo
Diffraction source	SSRL 12-2	SSRL 7-1	SSRL 12-2	SSRL 7-1	LCLS MFX	LCLS MFX	LCLS MFX	APS 14BM-C
Wavelength (Å)	0.827	0.975	0.827	0.975	1.305	1.305	1.305	0.900
Temperature (K)	274	277	274	277	298	298	298	100
Detector	Pilatus 6M	ADSC Q315	Pilatus 6M	ADSC Q315	Rayonix MX340-XFEL	Rayonix MX340-XFEL	Rayonix MX340-XFEL	ADSC Q315
Space group	P2 <sub>1</sub>	P2 <sub>1</sub>	P2 <sub>1</sub>	C2	P2 <sub>1</sub>	P2 <sub>1</sub>	P2 <sub>1</sub>	P2 <sub>1</sub>
a, b, c (Å)	57.24 58.03 69.09	57.15 57.97 69.09	57.04 57.90 69.11	72.11 59.74 56.13	56.88 57.68 68.78	56.77 57.42 68.79	56.81 57.64 68.76	56.58 56.47 68.23
α, β, γ (°)	90.00 112.83 90.00	90.00 112.77 90.00	90.00 112.55 90.00	90.00 115.86 90.00	90.00 112.74 90.00	90.00 112.74 90.00	90.00 112.74 90.00	90.00 112.49 90.00
Mosaicity (°)	0.08	0.08	0.08	0.07	N/A <sup>5</sup>	N/A <sup>5</sup>	N/A <sup>5</sup>	0.27
Resolution range (Å)	39.04-1.20 (1.22-1.20)	42.87-1.15 (1.17-1.15)	38.96-1.30 (1.32-1.30)	35.45-1.10 (1.12-1.10)	20.13-1.55 (1.57-1.55)	20.09-1.55 (1.57-1.55)	20.1-1.55 (1.57-1.55)	37-1.05 (1.09-1.05)
Total no. of observations	363112 (16358)	517060 (15585)	327591 (13542)	224032 (2017)	3032726 (18818)	3185312 (16342)	2648001 (38049)	1077211 (79769)
No. of unique observations	126373 (5922)	145885 (6657)	100249 (4568)	84423 (1216)	60075 (2983)	60053 (2970)	60082 (2988)	179423 (17341)
Completeness (%)	97.4 (92.7)	98.9 (91.2)	98.1 (90.1)	97.2 (95.9)	99.9 (99.8)	99.9 (99.4)	99.9 (100)	97.1 (94.2)
Multiplicity	2.9 (2.8)	3.5 (2.3)	3.3 (3.0)	2.7 (2.0)	50.5 (6.3)	53.0 (5.5)	44.1 (12.7)	6.0 (4.6)
$\langle I/\sigma(I) \rangle$	10.4(1.8)	12.5 (0.8)	9.1 (1.2)	9.7 (1.4)	60.5 (2.0)	58.4 (1.8)	73.1 (3.4)	22.8 (2.1)
CC <sub>1/2</sub> <sup>2</sup>	0.991 (0.225)	0.999 (0.488)	0.996 (0.318)	0.999 (0.690)	0.962 (0.16)	0.963 (0.14)	0.937 (0.36)	N/A <sup>4</sup>
R <sub>meas</sub> (R <sub>split</sub> for XFEL data) <sup>3</sup>	0.072 (1.689)	0.059 (0.959)	0.066 (1.513)	0.045 (0.545)	0.196 (0.862)	0.197 (0.905)	0.232 (0.658)	0.07 (0.70)

Values for the highest resolution bins are shown in parenthesis

<sup>1</sup> RT, Room temperature synchrotron radiation collection; XFEL, X-ray free electron laser<sup>2</sup> CC<sub>1/2</sub> (16) was used to determine the high resolution cutoff.<sup>3</sup> R<sub>split</sub> is provided only for XFEL serial crystallographic data<sup>4</sup> Dataset from PDB 3NON, processed before the introduction of CC<sub>1/2</sub><sup>5</sup> N/A=not applicable for serial crystallographic data

**Table S3: Crystallographic Refinement Statistics**

Model	WT ICH RT <sup>1</sup> (less oxidized)	WT ICH RT <sup>1</sup> (more oxidized)	G150A ICH	G150T ICH	WT ICH XFEL: Free <sup>1</sup>	WT ICH XFEL: 15 sec Thioimida- te <sup>1</sup>	WT ICH XFEL: 5 min <sup>1</sup>	WT ICH RT <sup>1</sup> (less oxidized) qFit model	WT ICH cryo with helix disorder
PDB code	6NI6	6NI7	6NI5	6NI4	6NPQ	6UND	6UNF	6NI9	6NJA
Temperature (K)	274	277	274	277	298	298	298	274	100
Refinement program	PHENIX 1.9	PHENIX 1.9	PHENIX 1.9	PHENIX 1.9	PHENIX 1.16	PHENIX 1.16	PHENIX 1.16	PHENIX 1.9	PHENIX 1.9
Resolution range (Å)	31.84- 1.20	38.53- 1.15	33.56- 1.30	35.14- 1.10	20.13- 1.55	20.09- 1.55	17.46- 1.55	31.84- 1.20	37.82- 1.05
Completeness (%)	95.17	98.87	97.83	97.16	99.93	99.86	99.96	95.00	97.11
No. of reflections	123572	145829	99966	84275	59628	59214	59498	123572	179399
No. of reflections, test set	6203	7300	4970	4186	2002	1986	1995	6203	8979
R <sub>work</sub>	0.1140 (0.2281)	0.1128 (0.2633)	0.1192 (0.2745)	0.1098 (0.2294)	0.1595 (0.3110)	0.1633 (0.3220)	0.1693 (0.2698)	0.1078 (0.2207)	0.1170 (0.2105)
R <sub>free</sub>	0.1398 (0.2611)	0.1353 (0.2607)	0.1519 (0.3159)	0.1283 (0.2332)	0.1865 (0.3319)	0.1908 (0.3141)	0.1945 (0.2843)	0.1402 (0.2628)	0.1342 (0.2487)
No. of non-H atoms									
Protein	4486	4446	4892	1868	3475	3449	3500	6192	4551
Water	342	323	323	149	298	269	270	382	484
Total	4828	4769	5215	2017	3773	3718	3770	6574	5035
Average R.M.S. deviations									
Bonds (Å)	0.007	0.008	0.014	0.011	0.005	0.005	0.007	0.011	0.009
Angles (°)	0.909	1.020	1.290	1.376	0.776	0.778	0.854	1.399	1.111
Average B factors (<B <sub>iso</sub> >, Å <sup>2</sup> )									
Protein	17.34	19.57	21.12	17.21	26.44	25.79	25.20	15.92	11.91
Water	36.77	37.40	39.73	31.30	42.17	40.52	43.44	36.74	26.43
Average ADP anisotropy <sup>2</sup>									
Protein	0.396	0.481	0.400	0.502	0.582	0.565	0.583	0.394	0.407
Water	0.327	0.415	0.353	0.439	1	1	1	0.354	0.408
MolProbity clashscore	1.1	2.2	4.1	0.8	1.7	2.3	1.3	2.4	3.2
Ramachandran plot									
Outliers (%)	0.5	0.3	0.5	0.0	0.4	0.4	0.4	0.3	0.3
Allowed (%)	1.4	1.4	2.0	1.2	1.3	1.1	1.8	1.1	1.9
Favored (%)	98.1	98.3	97.5	98.8	98.2	98.5	97.8	98.6	97.8

Values for the highest resolution bin shown in parenthesis

<sup>1</sup> RT, Room temperature synchrotron radiation collection; XFEL, X-ray free electron laser

<sup>2</sup> Anisotropy is defined as the ratio of the smallest to largest eigenvalue of the ADP tensor

## Supplementary Results

**Propagation of cysteine-gated conformational changes across the ICH dimer.** To characterize the extent of the conformational response of the entire ICH dimer to the modification of Cys101, we calculated an  $F_o(\text{SR}) - F_o(\text{XFEL}_{\text{Free}})$  isomorphous difference map, phased with a structural model obtained from the XFEL data set. The  $F_o(\text{SR}) - F_o(\text{XFEL}_{\text{Free}})$  isomorphous difference map provides an unbiased view of differences in molecular conformation between two data sets, reporting specifically on changes in ICH that occur in response to oxidation of Cys101. A  $F_o(15\text{s}) - F_o(\text{XFEL}_{\text{Free}})$  map calculated using the thioimidate dataset after 15 s of mixing and the dataset prior to introduction of substrate (Free) reveals similar features to those seen in the  $F_o(\text{SR}) - F_o(\text{XFEL}_{\text{Free}})$  map (SI Appendix Figure S4), signifying that the widespread dynamic response observed in  $F_o(\text{SR}) - F_o(\text{XFEL}_{\text{Free}})$  difference map is common to different types of Cys101 modification.

We further examined the dynamical communication across the dimer interface in ICH using CONTACT network analysis of the electron density maps. CONTACT elucidates pathways of collective amino acid main- and sidechain displacements through mapping van der Waals conflicts that would result from sidechain conformational disorder if correlated motions are not considered (17). CONTACT identified a large network of correlated residues in protomer A (with the mobile helix) that connects with a smaller network in protomer B (Figure 3e), corroborating the isomorphous difference map. The key residues in CONTACT analysis that bridge the dimer interface are Tyr181 and Thr153 (Figure 4e), which are also key residues identified in the isomorphous difference map.

We computed rigid cluster decompositions of ICH corresponding to the unshifted (XFEL) and shifted (SR) conformations. We removed all alternate conformations in the three crystal structures, retaining only conformations corresponding to the unshifted state in the XFEL structure, and the shifted state in the SR structure. Waters were retained. These structures were protonated at pH 7.0 and minimized under the OPLS3 force field using the Schrödinger 2018-3 software suite [Schrödinger Suite 2018-3 Protein Preparation Wizard; Schrödinger, LLC, New York, NY, 2016]. We then used our KGS software suite (18) to carry out rigidity analysis, using hydrogen bonds stronger than -1 kcal/mol and hydrophobic interactions as constraints. In the XFEL structure, the Cys101-Ile152 H-bond was added as a constraint in both protomers. In the SR structure, the Cys101-Ile152 H-bond was included only in the B protomer.

All structures show a largely rigid core (SI Appendix Figure S5), although the largest cluster (blue) is slightly bigger in the SR structure than in the XFEL structure. The IJ linkers (opaque) are rigid in the XFEL structure (SI Appendix Figure S5a), while linker IJ<sub>B</sub> melted in the SR structure, concomitant with the shifted helix H<sub>A</sub> (SI Appendix Figure S5b), signifying that the loss of a non-covalent interaction in response to Cys101 oxidation allosterically propagates across the protein. Notably, we found that the IJ linkers are the first major structural elements to melt once weaker H-bonds are excluded from the analysis (SI Appendix Figure S5c).

### Kinematic Flexibility Analysis (KFA) of the conformational ensembles modulated by the C101-I152 hydrogen bond.

In KFA (19), a protein is represented as a kinematic linkage, with rotatable bonds  $\mathbf{q}$  as degrees of freedom (DoFs) and hydrogen bonds and hydrophobic interactions as constraints. The constraints introduce cycles in the kinematic linkage, which impose coordinated motion on the degrees of freedom to maintain the constraints. These coordinated motions take place on a

lower dimensional manifold of conformation space. Briefly,  $m$  constraints in a protein with  $d$  degrees of freedom define a constraint manifold

$$\mathcal{Q} = \{\mathbf{q} \in \mathbb{T}^d | \Phi(\mathbf{q}) = \mathbf{0} \in \mathbb{R}^m\}$$

Formally differentiating with respect to time yields a linear relationship between instantaneous changes in the DoFs ( $\dot{\mathbf{q}}$ , ‘velocities’) and corresponding changes in the constraints:

$$\frac{d\Phi}{dt} = \mathbf{J}\dot{\mathbf{q}}$$

The matrix  $\mathbf{J}$  is known as the constraint Jacobian. By way of a singular value decomposition  $\mathbf{JV} = \mathbf{U}\Sigma$ , we obtain an expression  $\mathbf{Jv}_i = \sigma_i \mathbf{u}_i$  relating a change in molecular conformation  $\mathbf{v}_i$  to a change in the geometry  $\mathbf{u}_i$  of all hydrogen bonds and hydrophobic constraints. Instantaneous changes of DoFs  $\mathbf{v}_i$  that do not affect hydrogen bonds and hydrophobic constraints lie in the nullspace of  $\mathbf{J}$ :  $\mathbf{Jv}_i = \mathbf{0}$ . Normalized singular values  $\sigma_i$  are proportional to the magnitude of internal hydrogen bond energy changes for motions along each mode  $i$ , with the constant of proportionality equal to 3.24 kcal/mol, independent of the mode. This leads to a formal, dimensionless expression for changes in the free energy  $\Delta F_i = \sigma_i - c_T s_i$ , for each motion mode. Here,

$$s_{v_i} = \frac{1}{d} \exp \left\{ - \sum_{j=1}^d \kappa_{ij} \log (\kappa_{ij}) \right\}$$

is the normalized exponential of the Shannon entropy calculated for each motion mode, and

$$\kappa_{ij} = \frac{v_{ij}^2}{\sum_{j=1}^d v_{ij}^2}$$

are the normalized velocities for each mode  $i$ , and  $c_T = 1$  is a constant. The Shannon entropy  $s_{v_i}$  represents how contributions of DoFs for each mode are distributed over the protein (*mode collectivity*) and renders  $\Delta F_i \in [-1,1]$  for  $c_T = 1$ . Thus,  $\Delta F_i$  balances enthalpic (constraint relaxation) contributions and conformational entropy (collectivity of motions) for each mode. For details, see (19).

We compared the spectrum of motion modes in the case where both protomers of the XFEL structure are subject to the Cys101-Ile152 hydrogen bond as a constraint, to the case where only the B protomer has the Cys101-Ile152 hydrogen bond as a constraint. This situation corresponds to an event of instantaneous disruption of the H-bond in one protomer. To investigate how motion modes changed upon disruption of the H-bond, we identified ten modes from a surface of near-constant free energy changes that are most dissimilar between the two scenarios. More precisely, we calculated the matrix product  $\mathbf{D} = \mathbf{V}_B^T \mathbf{V}_{A\&B}$ , where  $\mathbf{V}_{A\&B}$  are the right singular vectors of the XFEL structure when the Cys101-Ile152 H-bond is present in both protomers, versus  $\mathbf{V}_B$  for the B protomer only. Note that  $\mathbf{D}$  is orthonormal, and that an entry  $|d_{ij}|$  near 1 denotes that  $\mathbf{v}_{B,i}$  and  $\mathbf{v}_{A\&B,j}$  are motions along the same direction in conformation space, whereas  $|d_{ij}|$  near 0 denotes orthogonal motions (SI Appendix Figure S6).

We then identified motion modes that significantly changed or shifted in the spectrum between **B** and **A&B**. Those motions will have a different effect on the geometry/energy  $\mathbf{u}_i$  of all hydrogen bonds and hydrophobic constraints and are differentially accessible to the protein after disruption of the Cys101-Ile152 hydrogen bond. Modes in the nullspace of  $\mathbf{J}$  (SI Appendix Figure S6, mode number  $> \sim 1,450$  corresponding to vanishing singular values) are least

conserved between  $V_B$ , and  $V_{A\&B}$ , mostly because the nullspace basis is not unique. These modes are generally localized, with low collectivity and unfavorable free energy changes. Therefore, we first identified a set of 100 modes with lowest free energy, from which we then selected the top ten modes with least overlap to any other mode, i.e., for which  $\max_j |d_{ij}|$  is smallest. The free energy and mode overlap of these ten modes are indicated with stars in SI Appendix Figure S6. We then perturbed the XFEL structure with one individual step along each of these ten modes  $v_i$  with unit step size to obtain an ensemble in which the root-mean-squared fluctuations represent the overall change in mobility due to the additional or missing hydrogen bond.

KFA can provide an explicit basis for orthogonal protein motion modes coupled to energetic penalties incurred by perturbing the constraint network. Using KFA to understand how the active site Cys101-Ile152 hydrogen bond modulates conformational dynamics revealed that changes in protein flexibility between the unshifted and shifted conformations are concentrated in the IJ linkers (SI Appendix Figure S6). In contrast to traditional molecular rigidity analysis (SI Appendix Figure S5), KFA can rank-order protein motions by the magnitude of free energy changes calculated from non-covalent interactions and molecular rigidity (see details above). We analyzed how motion modes corresponding to the lowest free energies in the structure without Cys101 modification change when the H-bond is intact in both A and B protomers ( $C101-I152_{A\&B}$ ) to when this H-bond is disrupted in protomer A ( $C101-I152_B$ ). These altered motion modes are the ones most affected by disruption of the hydrogen bond. Among the top 100 modes with lowest free energy in each of  $Cys101-Ile152_{A\&B}$  and  $Cys101-Ile152_B$ , we identified ten modes that showed least overlap between the  $Cys101-Ile152_{A\&B}$  and  $Cys101-Ile152_B$  (SI Appendix Figure S6). We then computed root mean square fluctuations (RMSF) resulting from sampling these motion modes (SI Appendix Figure 6c). Interestingly, we observed that the perturbations in the H-bonding network are propagated primarily to the IJ-linkers and helix J, consistent with the MD simulations. Strikingly, the largest RMSFs within the IJ linkers were observed near the active site in the opposite protomer, suggesting that the two sites are in allosteric communication. Identical analyses on the B-protomer hydrogen bond or the XFEL structure yielded similar results. By contrast, ten randomly selected motion modes lead to conformational changes distributed non-specifically throughout the dimer (SI Appendix Figure S6).

Our results indicate that the conformational changes upon Cys101-Ile152 H-bond modification in the synchrotron structure correspond to later steps in the catalytic cycle, allowing helix motion that facilitates intermediate hydrolysis and product release. At the same time, increased allosteric transmission during these later steps may contribute to kinetic heterogeneity in the two active sites of the ICH dimer.

### Supplementary Discussion

Cysteine modification-gated conformational changes in ICH alter the active site environment, promoting progress along the reaction coordinate. ICH catalyzes a reaction that can be divided into an early phase dominated by nucleophilic attack of Cys101 at the electrophilic carbene-like carbon of its isocyanide substrate and a later phase dominated by hydrolysis of the thioimidate intermediate to release the N-formamide product (Figure 1b). The early phase requires a reactive cysteine residue to initiate nucleophilic attack, while the subsequent phase requires water attack at the thioimidate and weaker nucleophilicity of Cys101 (i.e. a better leaving group) to release the product. These two phases of ICH catalysis place conflicting demands on the physical properties of Cys101. The divergent pre-steady state kinetics of the G150A and G150T mutants suggest a model where the strained helical conformation of ICH has the highest competence for the initial isocyanide attack by Cys101,

forming the thioimidate intermediate (Figure 1b). This is also consistent with the diminished propensity of Cys101 for photooxidation in G150T, where the helix is constitutively shifted, suggesting that Cys101 is less reactive in this environment (Figure 4b). After formation of the thioimidate, the helix samples the shifted conformation due to weakening of the Ile152-Cys101 H-bond, dynamically remodeling the ICH active site (Figures 1b, 4e) and permitting water entry. This transient remodeling is required for hydrolysis of the thioimidate intermediate, because the active site containing the intermediate is occluded and does not contain room enough for a water to enter without motion. Water attack at the C-S bond of the thioimidate is proposed to form a tetrahedral intermediate (Figure 1b). At this point, the H-bond between Cys101 and Ile152 that restrains the strained conformation of helix H can reform, thereby stabilizing the nascent Cys101-S<sup>-</sup> and making it a better leaving group. With the strained helical conformation restored, the product is released and leaves the active site poised for another cycle of catalysis (Figure 4e).

The G150A/T mutants modulate helical dynamics and thus allow us to determine if the non-equilibrium helical motions that we observe in the thioimidate intermediate XFEL structure are incidental to or important for catalysis. Synchrotron X-ray crystallographic data indicate that the G150A mutation enhances sampling of shifted helical conformations even in the absence of Cys101 modification, and this shifted conformation is further populated once the Cys101-Ile152 H-bond is weakened by Cys101-SOH formation (Figure 4a). In addition, G150A ICH accumulates a spectrally distinct 335 nm species that likely corresponds to the thioimidate intermediate detected by XFEL crystallography (Figure 4d). Our interpretation of these data is that the thioimidate intermediate accumulates in G150A ICH owing to an impaired resetting of the strained helical conformation, which reduces the rate of thioimidate hydrolysis and enzyme turnover. Consistent with the pre-steady state kinetic data, this kinetic model for G150A ICH predicts that the early chemical steps promoted by the strained conformation of helix H would not be impaired by the mutation but that the steady-state rate would be significantly diminished. In contrast, the G150T mutation causes a constitutively shifted helix, reducing rates of both initial Cys101 attack at the isocyanide carbon atom in the first chemical step and thioimidate hydrolysis in later steps, as evidenced by the lower burst and steady state rates of G150T ICH (Figure 4c, SI Appendix Table S1). Therefore, the G150A and G150T mutations have divergent effects on the early steps of ICH catalysis but similar detrimental effects on the later, rate-limiting steps.

Modulation of protein dynamics is a powerful way to regulate protein function, as has been characterized in various systems. To our knowledge, ICH is the first example of a non-disulfide cysteine modification regulating functional protein conformational dynamics. Nevertheless, conceptually similar examples of gated conformational dynamical changes exist. Redox-gated changes in flavoprotein structure and dynamics may play a major role in electron transfer by these proteins (20), and similar electron- or charge-coupled gating events occur in diverse systems (21-23). Photoactivatable tags that modulate sampling of active enzyme conformations have been used to create catalytically enhanced enzymes (24). In the DJ-1 superfamily to which ICH belongs, Cys106 oxidation to Cys106-SO<sub>2</sub><sup>-</sup> in DJ-1 results in little change in global protein conformation but stabilizes the protein by over 12°C (25). This stabilization is thought to be due to a strong (2.47 Å) hydrogen bond between Cys106-SO<sub>2</sub><sup>-</sup> and Glu18 that forms upon oxidation, reducing protein dynamics and stabilizing the protein.

More generally, transient covalent modification of proteins changes their potential energy surface. Therefore, various covalently modified species of a protein in the cell are likely to be dynamically distinct, providing another mechanism of diversifying protein function. The many potential covalent modifications of cysteine make this residue of particular importance for

understanding how cellular signaling states, metabolite pools, and stress conditions couple to functional protein dynamics through the modification of amino acids in proteins. Future work on ICH and other cysteine-containing proteins will illuminate the diverse mechanisms by which cysteine-gated conformational changes can regulate protein function.

### Supporting Information References

1. Lakshminarasimhan M, Madzelan P, Nan R, Milkovic NM, & Wilson MA (2010) Evolution of new enzymatic function by structural modulation of cysteine reactivity in *Pseudomonas fluorescens* isocyanide hydratase. *J. Biol. Chem.* 285(38):29651-29661.
2. Kabsch W (2010) Integration, scaling, space-group assignment and post-refinement. *Acta Crystallogr. D, Biol. Crystallogr.* 66(Pt 2):133-144.
3. Otwinowski Z & Minor W (1997) Processing of X-ray diffraction data collected in oscillation mode. *Methods Enzymol.* 276:307-326.
4. Sierra RG, et al. (2016) Concentric-flow electrokinetic injector enables serial crystallography of ribosome and photosystem II. *Nature Methods* 13(1):59-62.
5. Mariani V, et al. (2016) OnDA: online data analysis and feedback for serial X-ray imaging. *J. Appl. Crystallogr.* 49(Pt 3):1073-1080.
6. Sauter NK, Hattne J, Grosse-Kunstleve RW, & Echols N (2013) New Python-based methods for data processing. *Acta Crystallogr. D, Biol. Crystallogr.* 69(Pt 7):1274-1282.
7. Uervirojnangkoorn M, et al. (2015) Enabling X-ray free electron laser crystallography for challenging biological systems from a limited number of crystals. *eLife* 4.
8. Adams PD, et al. (2010) PHENIX: a comprehensive Python-based system for macromolecular structure solution. *Acta Crystallogr. D, Biol. Crystallogr.* 66(Pt 2):213-221.
9. Schomaker V & Trueblood KN (1968) On Rigid-Body Motion of Molecules in Crystals. *Acta Crystallogr. B* 24:63-76.
10. Emsley P & Cowtan K (2004) Coot: model-building tools for molecular graphics. *Acta Crystallogr. D, Biol. Crystallogr.* 60(Pt 12 Pt 1):2126-2132.
11. Davis IW, et al. (2007) MolProbity: all-atom contacts and structure validation for proteins and nucleic acids. *Nucleic Acids Res.* 35(Web Server issue):W375-383.
12. Goda M, Hashimoto Y, Shimizu S, & Kobayashi M (2001) Discovery of a novel enzyme, isonitrile hydratase, involved in nitrogen-carbon triple bond cleavage. *J. Biol. Chem.* 276(26):23480-23485.
13. Case DA, et al. (2005) The Amber biomolecular simulation programs. *J. Comput. Chem.* 26(16):1668-1688.
14. Wang J, Wang W, Kollman PA, & Case DA (2006) Automatic atom type and bond type perception in molecular mechanical calculations. *J. Mol. Graph. Model.* 25(2):247-260.
15. Eastman P & Pande VS (2015) OpenMM: A Hardware Independent Framework for Molecular Simulations. *Comput. Sci. Eng.* 12(4):34-39.
16. Karplus PA & Diederichs K (2012) Linking crystallographic model and data quality. *Science* 336(6084):1030-1033.
17. van den Bedem H, Bhabha G, Yang K, Wright PE, & Fraser JS (2013) Automated identification of functional dynamic contact networks from X-ray crystallography. *Nature Methods* 10(9):896-902.
18. Budday D, Leyendecker S, & van den Bedem H (2015) Geometric analysis characterizes molecular rigidity in generic and non-generic protein configurations. *J. Mech. Phys. Solids* 83:36-47.
19. Budday D, Leyendecker S, & van den Bedem H (2018) Kinematic Flexibility Analysis: Hydrogen Bonding Patterns Impart a Spatial Hierarchy of Protein Motion. *J. Chem. Inf. Model.* 58(10):2108-2122.

20. Toogood HS, Leys D, & Scrutton NS (2007) Dynamics driving function: new insights from electron transferring flavoproteins and partner complexes. *FEBS J.* 274(21):5481-5504.
21. Danyal K, Mayweather D, Dean DR, Seefeldt LC, & Hoffman BM (2010) Conformational gating of electron transfer from the nitrogenase Fe protein to MoFe protein. *J. Am. Chem. Soc.* 132(20):6894-6895.
22. Catterall WA, Wisedchaisri G, & Zheng N (2017) The chemical basis for electrical signaling. *Nat. Chem. Biol.* 13(5):455-463.
23. Liu Y, *et al.* (2017) A pH-gated conformational switch regulates the phosphatase activity of bifunctional HisKA-family histidine kinases. *Nat. Commun* 8(1):2104.
24. Agarwal PK, Schultz C, Kalivretenos A, Ghosh B, & Broedel SE (2012) Engineering a Hyper-catalytic Enzyme by Photoactivated Conformation Modulation. *J. Phys. Chem. Letters* 3(9):1142-1146.
25. Lin J, Prahlad J, & Wilson MA (2012) Conservation of oxidative protein stabilization in an insect homologue of parkinsonism-associated protein DJ-1. *Biochemistry* 51(18):3799-3807.